Development of semi-solid alkaline flow battery

by
Thaneer Malai Narayanan

B. Eng. Mechanical Engineering
Keio University, 2016

SUBMITTED TO THE DEPARTMENT OF MECHANICAL ENGINEERING IN PARTIAL FULFILLMENT OF THE REQUIREMENTS FOR THE DEGREE OF

MASTER OF SCIENCE IN MECHANICAL ENGINEERING
AT THE
MASSACHUSETTS INSTITUTE OF TECHNLOGY

SEPTEMBER 2018

Signature redacted

Signature of Author:.....
Department of Mechanical Engineering
August 10, 2018

Signature redacted

Certified by:.....
Yang Shao-Horn
W.M. Keck Professor of Energy
Department of Mechanical Engineering
Thesis supervisor

Signature redacted

Accepted by:.....
Rohan Abeyaratne
Chairman, Department Committee on Graduate Theses
Department of Mechanical Engineering

Development of semi-solid alkaline flow battery

by
Thaneer Malai Narayanan

Submitted to Department of Mechanical Engineering on August 10, 2018 in Partial Fulfilment of the Requirements for the Degree of Master of Science in Mechanical Engineering

ABSTRACT

Flow battery is an attractive energy storage system due to its ability to decouple power and energy outputs, and its less stringent geometric requirement. However, commercial flow battery technology suffers from low energy density (~40 $Wh/L_{catholyte}$), high membrane cost (~$ 500/m^2) and species crossover. One elegant method to overcome all this problems is utilize flowable semi-solid electrode. Although there have been several reports in the literature regarding performance of various semi-solid flow batteries, there is still lack of understanding on how to design the suspension electrode and its impact on flow cell design and performance. In this thesis, we emphasize on three main properties, namely stability, conductivity and flowability for high performing suspension electrode for Zn-Ni alkaline battery chemistry.

Firstly, we recognized interplay of forces acting on particles in a suspension electrode and designed suspending medium with jammed Carbopol© microgel structures to prevent sedimentation of the large particles. Secondly, we determined percolation threshold of conductive additive and investigated its effect on electrochemical performance of the semi-solid electrodes in a closed static cell. We found that conductive additive concentration should be well above percolation threshold to obtain maximum discharge capacity of Ni(OH)2. Thirdly, based on the understanding from conductivity and stability of the suspension, we designed catholyte (~ 5 M Ni(OH)2) and tested its electrochemical performance in a static cell. We were able to achieve energy density of 137 $Wh/L_{catholyte}$, about 3 times of commercial flow battery. We then assessed flowability of the suspensions. Catholyte and anolyte had yield stress of 204 Pa and 447 Pa respectively. We found that by choosing appropriate flow cell stack design energy loss due to pumping can be minimized to < 1% for continuous flow. Finally, flow cells were designed to test the electrochemical performance of these suspensions in an open system.

Thesis Supervisor: Yang Shao-Horn
Title: W.M. Keck Professor of Energy

Thesis Supervisor: Gareth McKinley
Title: School of Engineering Professor of Teaching Innovation

Acknowledgment

Both electrochemistry and rheology were a new experience for me. I would not have been able to complete this interdisciplinary work without the support of Professor Yang Shao-Horn and Professor Gareth McKinley. I would like to thank them not only for their technically expertise but also for their guidance on how to approach a new research topic and how to be a better researcher in general. I am also truly indebted to Yunguang and Michal, who have I have worked closely in this project. Their wide experience, intuition and know-hows were truly essential in shaping up this interdisciplinary project. My thanks also goes to EEL lab members, who have maintained very energetic and joyful lab culture. This work would also not been possible without the help of graduate students from HML in using the rheometer and in rheology in general. I also would like to take this opportunity to thank ENI for their sponsorship and continued interest and confidence in this project. Special thanks goes to my friends here in US, back home in Malaysia and in Japan for their unwavering emotional support throughout this two years. Finally, to my mother, father, sisters and their families, none of this would not have been possible without all your encouragement and love.

Table of Contents

List of Figures

1. Introduction

1.1 Electrochemical energy storage systems for the grid

In the recent years, penetration of renewable energy sources in global market has been constantly increasing[1].

Figure 1 shows growth in renewable energy capacity addition for various technologies in the global market. Between the years 2017-2022, it is expected that capacity additions from energy sources such as wind and sunlight to occupy 82% of the new market. Renewable energy sources are attractive not only for its ability to reduce greenhouse gas emissions, but also to reduce dependency of remote areas on fossil fuels and promote their growth through microgrids. One important aspect of electricity generation from renewable energy sources such as wind and sunlight is that, it requires energy storage systems due to its intermittent nature.

Selection of energy storage systems typically depend on their required storage time, required storage power[2]. Figure 2 shows conceptual positioning of various energy storage technologies according to their storage power and storage time. Technologies such as pumped hydro and compressed air energy storage system are more suited for high power (~ GW scale) and long storage time applications, due to their geographically restrictions. Both technologies require large reservoir to store pumped water and compressed air respectively. On the other hand, electrochemical energy-based energy storage systems are more compact and suited smaller power and shorter discharge time applications.

There are three types of electrochemical energy storage systems: battery, fuel cells and supercapacitors[3]. In this chapter, only battery will be focused as it is more relevant to the scope of study of this thesis. A battery converts electrical energy to/from chemical energy through redox reactions. During discharge the negative electrode undergoes oxidation, the positive electrode

undergoes reduction, and vice-versa during charge. And these two electrodes are separated by a separator which allows transport of ion from one electrode to the other to maintain electroneutrality, while preventing self-discharge or short-circuiting between the two electrodes. Energy storage capabilities of a particular electrochemical couple is determined by difference in Gibbs free energy of the electrochemical reaction ΔG as following equation.

$$\Delta G = -nFE \tag{1}$$

where n the number of electrons transferred per mole of reactants, F is the Faraday's constant equivalent to charge per mole of electron, and E is the electromotive force that drives the electric current[4].

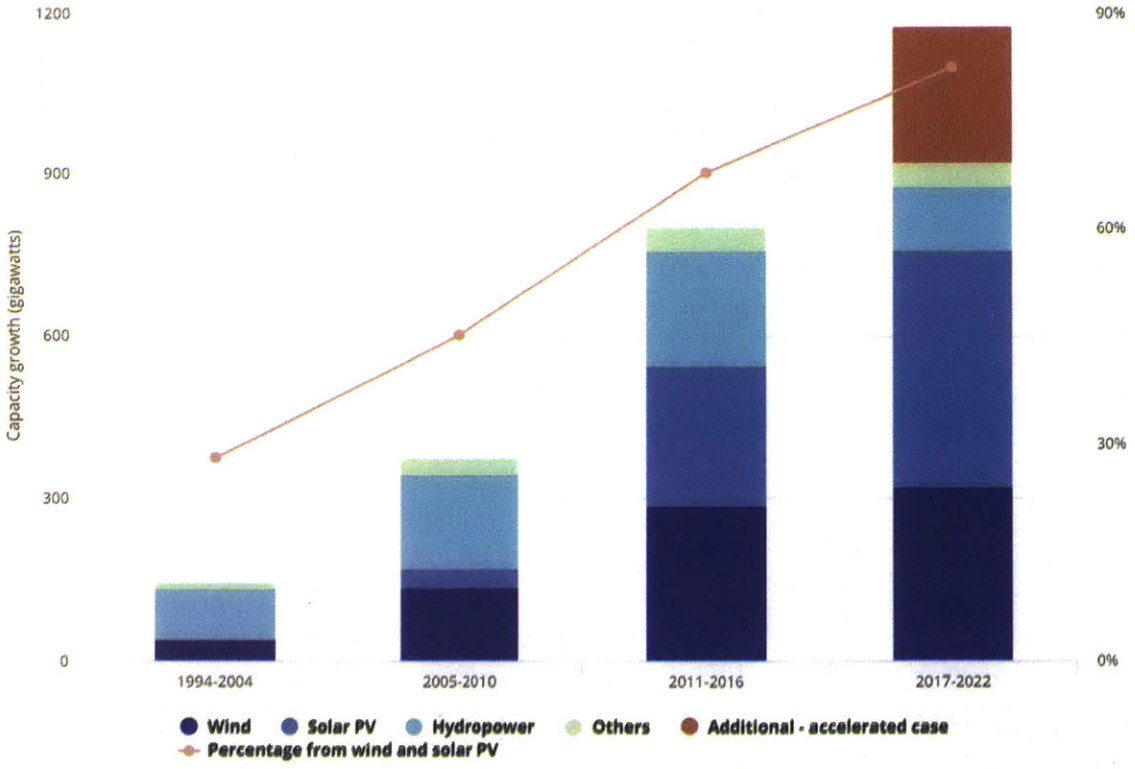

Figure 1: (left axis) Growth in renewable energy capacity addition for various renewable energy technology in global market. (right axis) Percentage of energy capacity addition from wind and solar PV.[5]

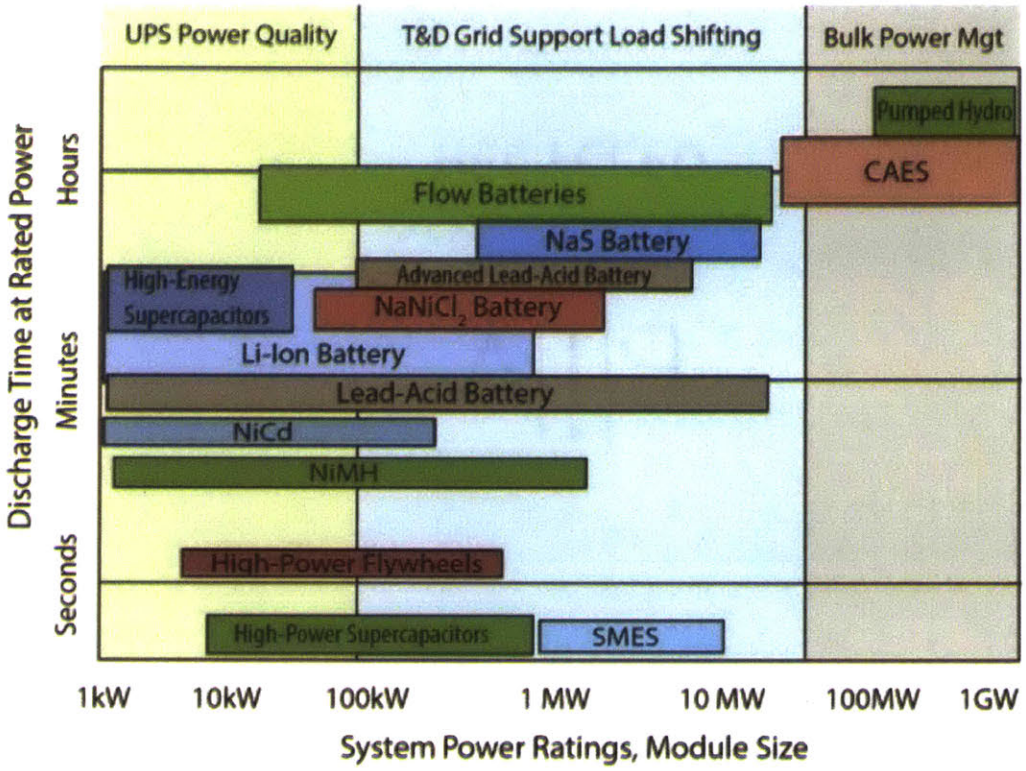

Figure 2: Conceptual positioning of various grid scale energy storage technologies with respect to their storage power and storage time[2]

Of all battery chemistries out in the market, probably, Li-ion battery is the most popular and most commonly used type, due to its high energy density and high specific energy (large difference in ΔG per volume and mass of the reactants respectively). Conventional architecture of Li-ion battery is shown in Figure 3. In this architecture all the active materials are enclosed in a case. Although this is simple and compact, they have poor scalability. Poor scalability of this

architecture is due the fixed ratio of mass of inactive components of the battery (case, separator, current collector etc.) to mass of active components. For example, in a typical Li-ion battery system, the inactive components compose ~ 30 to 50 % of the total mass of the battery[6]. Hence, if one is to double the energy or power output of the battery, the cost of these inactive materials will double too.

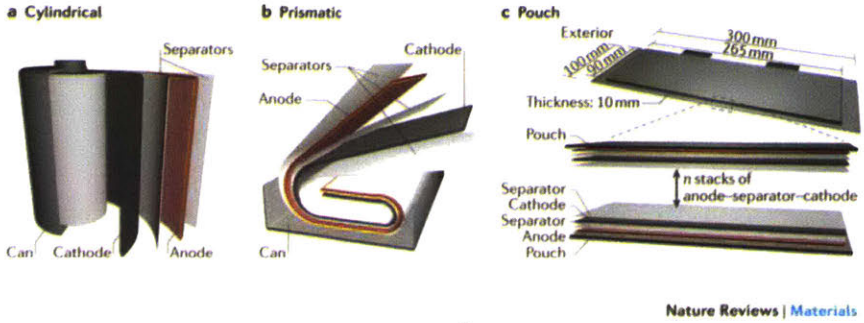

Figure 3: Conventional Li-ion battery architectures[7]

On the other hand, if the battery architecture is open and the active material is transported into the stack to be charged or discharged, as shown in Figure 4, the ratio of mass of inactive components of the battery (case, separator, current collector etc.) to mass of active components can be decoupled. This type of battery is called flow battery, derived from the fact that the active material is flowed into the stack. Hence, the battery's energy output, power output and cost can be scaled independently[8,9]. Energy output of the battery is dependent on the size of the tank and power output is dependent on the area of the flow stack. And, cost of the battery per kWh decreases with increasing time of battery discharge or energy output of the battery. This is because cost of inactive materials are minimized. Cost comparison per kWh for conventional Li-ion and flow battery is shown in Figure 5.

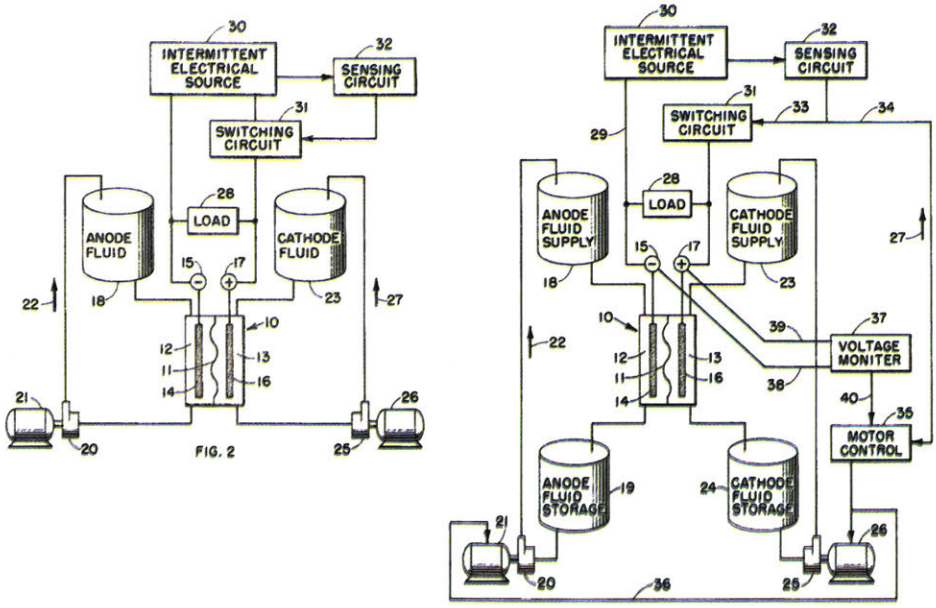

Figure 4: Architecture of flow battery, with two (left) or four (right) tanks as described by Thaller 1975.[10]

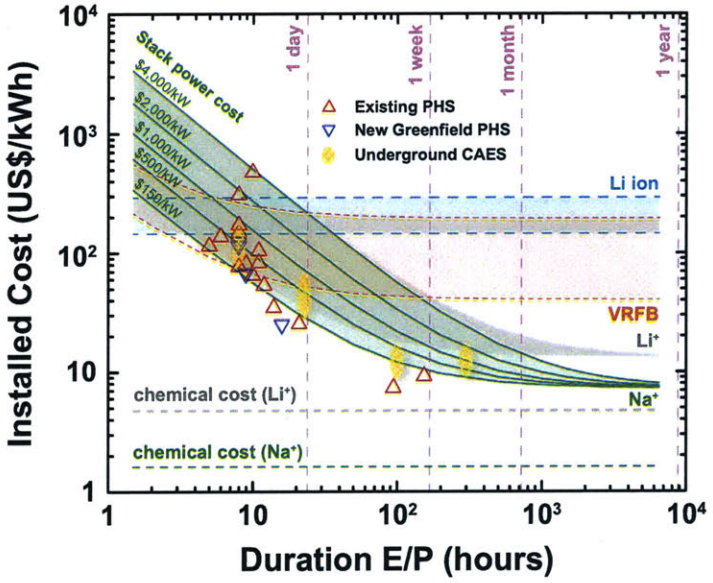

Figure 5: Cost comparison between Li-ion battery and flow batteries. At long discharge hours, the cost ($/kWh) reduces to cost of the active materials.[11]

First practical all-liquid flow battery was introduced by researchers at NASA in 1970's using Fe(II)/Fe(III) and Cr(II)/Cr(III) chemistry[10]. However, the kinetics of positive electrode reaction is sluggish, and required introduction of catalysts such as bismuth[8]. In 1986, Skyllas-Kazacos reported first vanadium redox flow battery (VRFB)[12]. The anodic half reaction is

$$V^{2+} \rightleftharpoons V^{3+} + e \tag{2}$$

with a potential of -0.255 vs SHE[13]. And the cathodic half reaction is

$$VO^{2+} + H_2O \rightleftharpoons VO_2^+ + 2\,H^+ + e^- \tag{3}$$

with a potential of -1.004 vs SHE[13]. The battery uses concentrated H_2SO_4 as electrolyte to increase the conductivity. One of the two most common problems still faced by VRFB is low solubility of the vanadium species in the sulfuric acid electrolyte and its requirement for narrow range of temperature to prevent precipitation[8,14]. The state-of-the-art electrolyte uses mixed H_2SO_4 and HCl electrolyte, which increases solubility of *V*(V) species up-to 2.5 M and widens the operational range to -5 to + 50°C.[13] Even with mixed H_2SO_4 and HCl electrolyte, the energy density of flowable catholyte is only ~40 $Wh/L_{catholyte}$.[13,15] Low energy density leads to increased capital cost for storage and also narrowed application space, as it won't be able to overcome energy density of conventional Li-ion battery (> 250 $Wh/L_{both\ electrodes}$).[8]

Another problem with all liquid flow battery such as VRFB is the cross-over of the soluble species. Strategies like, using ion-exchange membrane and periodic electrolyte reconstitution are used to overcome this issue. However, this leads to other practical problems such as increased cost of the stack, as ion-exchange membrane is expensive. For example, cation-exchange membrane Nafion© is projected to cost about $\$500/m^2$, as compared to $\$2/m^2$ for porous separator used in conventional such as Li-ion battery or alkaline batteries which uses solid active species[16].

1.2 Suspension electrode for semi-solid flow battery

One method to overcome low energy density and species cross-over problem in conventional flow battery vanadium is to utilize flowable solid electrodes. This type of battery is known as semi-solid flow battery, proposed by Chiang and co-workers in 2011[14]. As shown in Figure 6, suspension electrode in semi-solid flow battery is consists of conductive additive (typically carbon black), electrolyte, and solid active material. Now, the active material is not limited by the solubility of the active material in the electrolyte as all-liquid flow battery, but limited by packing of solid in the electrolyte. For a spherical particle, maximum packing density is about 60 – 70 vol%. Even if only 40 vol% is filled with active material particles, the molarity could reach upto ~17.7 M for a suspension with $Ni(OH)_2$ particles. This is ~7.2 times larger than molarity of VRFB catholyte. But, obviously, as more particles are added to the suspension, the resistance to flow increases too. This will be discussed in more detailed in the next chapter. Another advantage of using flowable suspension electrode is that, it eliminates cross-over of active species problem. Hence, this eliminates the need for expansive ion-exchange membrane. It is worth to note that prior to work by Duduta et al. suspension electrodes have already been used in commercial alkaline batteries such as Zn-MnO_2[17] and Zn-air batteries[18].

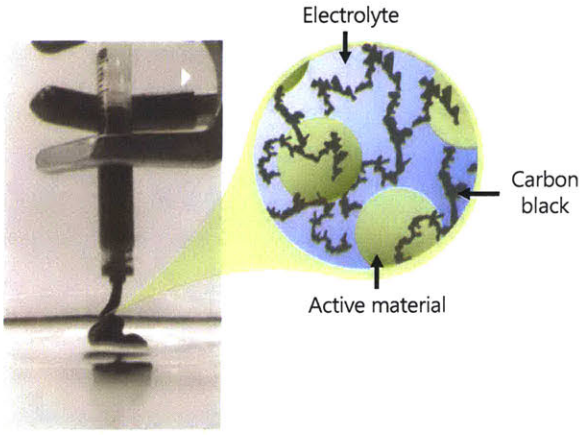

Figure 6: Schematic of suspension electrode used in semi-solid flow battery

Several batteries battery chemistries have been tested for semi-solid flow batteries. A summary of some milestones in using new chemistries for semi-solid flow batteries is shown in Table 1. Almost all of them have been largely limited to Li-ion or Li-S based chemistries and organic electrolytes. It is worth to note this summary omits reports on semi-solid electrochemical flow capacitors. Readers are suggested to refer to following reference for further studies on different types of semi-solid electrochemical energy storage systems[19].

Complex composition of suspension electrode makes it hard to distinguish how each component of the suspension affects the overall property. As mentioned previously, there are three main components in this flowable suspension, namely electrolyte, conductive additive, and active material. The role of electrolyte is to serve as ion conducting agent for the redox reaction and also to induce surface charge on the surface of carbon black particles. Presence of surface charge on carbon black particles will help to strengthen the attractive interactions among them to form a percolating conducting network[20]. When carbon black is dispersed in organic solvent with high dielectric constant such as mixture of ethylene carbonate and propylene carbonate (1:1), the KB was found to show negative surface charge. As salts LiTFSI or $LiPF_6$ is added (3 to 30 mM), the double layer is neutralized and zeta potential of the KB particles approached zero. This leads to flocculation and hence unstable suspension. When more salt is added the adsorption of Li^+ ion on the surface of carbon black inverts the surface potential to a positive value[21]. However, dispersing KB in aqueous electrolyte can be less straightforward due to hydrophobicity of carbon black surface. When KB is dispersed in water, the zeta potential is > 30mV below pH 8 and > -30 mV between pH 8 and 12[22]. Charge inversion at around pH 8, indicates some form of weak base functional group on the surface of KB. These results by Parant et al. explains why previous semi-solid flow battery[23] or flow capacitor[24–26] studies using mildly basic and acidic electrolytes were

able to create stable suspensions using KB. However, in the same study by Parant et al. different type of carbon black such as acetylene black (AB) was unable to disperse at any given pH[27]. This shows the importance of understanding the compatibility of carbon black and the electrolyte to ensure stable dispersion of solid particles in the suspension.[28]

Concentration of carbon black can also affect the properties of the suspension. When carbon black particles are able to achieve stable dispersion in the electrolyte, it will form multiple clusters. This network acts as a flexible wire between the active material and the current collector[29]. According to percolation theory, as the concentration of carbon black is increased, the size of the cluster gets larger. When one particular cluster gets infinitely large, the suspension is said to have reached percolation threshold.[30]

Figure 7 shows the images of "infinitely" large cluster above the percolation threshold 10 w% [31]. This 3-D percolating network then gives rise to bulk properties such as conductivity and elastic modulus.[32,33] For KB suspensions in 2.5 M Li-PS in triglyme, percolation threshold is reached at concentrations < 0.5 v% when investigated using conductivity[34]. This is surprising because percolation threshold for micrometer carbon black particles in organic solvent investigated using elastic modulus is about 5 v%.[35] Similar trend was observed by Richards et al. KB and Vulcan carbon black in propylene carbonate solvent.[33] It has been suggested this observation could be due to difference in nature of mechanical percolation and electrical percolation, where possibly there could be hopping of electrons from one cluster to the other without intimate mechanical contact.[33] Electrical percolation is favorable for suspension electrodes, as continuous carbon network is needed to transport electron to and from the active material at any given instant. However, mechanical percolation may not. This will be discussed in detail, in the next chapter.

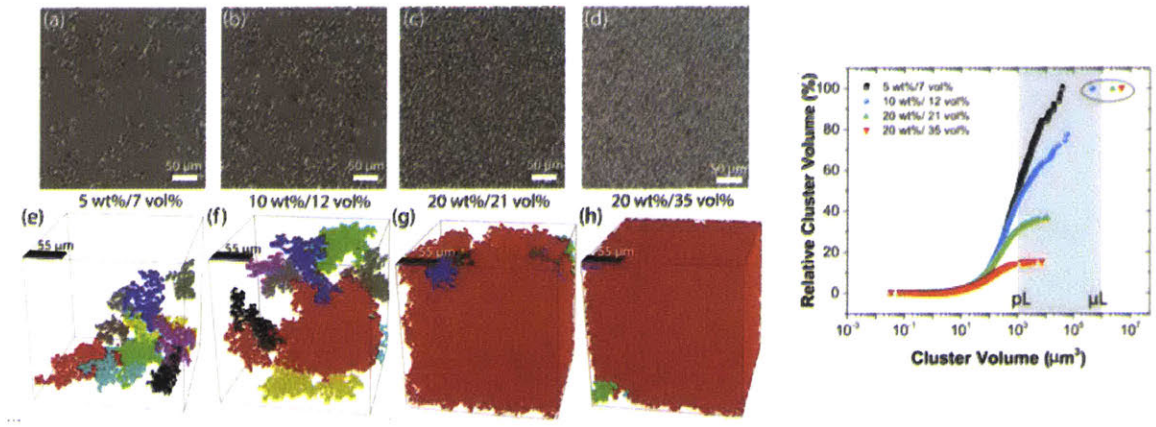

Figure 7: (left) 3D synchrotron X-ray tomography images of activated carbon (YP-50, particle size 1-10 micron) suspended in Na_2SO_4. (right) Above percolation threshold 10 w%, an "infinitely" large cluster is formed.[31]

Table 1: Summary of some milestones in chemistries used for semi-solid flow batteries

Negative electrode	**Conductive additive**	**Positive electrode**	**Conductive additive**	**Electrolyte**	**Notes**	**Reference**
Li4Ti5O5	KB	LiCoO2	KB	1.3 M $LiPF_6$ in proprietary alkyl carbonate	First suspension electrode for battery concept since Zn suspension for alkaline battery (refer 1.4)	Duduta et al. (2011) Adv. Energy Mater.
Li2Ti2(PO4)3	KB	LiFePO4	KB	1 M $LiNO_3$	Used aqueous electrolyte	Li et al. (2013) Phys. Chem. Chem. Phys.
Li foil	-	Si	KB	1 M $LiPF_6$ in EC:DMC (1:1)	Possibility of using electrode with high volume change	Hamelet (2013) J. Electrochem. Soc
Li foil	-	S	KB	0.5 M LiTFSI in TEGDME	Introduced soluble species for SSFB	Fan et al. (2014) Nano letters
Li foil	-	S	KB	0.2 M $LiClO_4$ + 0.1 $LiNO_3$ in DOL: DME (1:1)	KB impregnated with sulfur produces suspension with lower viscosity	Chen et al. (2015) Nat. Comms.
ZnO	KB	Ni(OH)2	KB + Ni powder	6 M KOH	Alkaline electrolyte	Liu & Wang (2015) J. Power Sources
Li foil	-	LiI + S	KB	0.2 M $LiClO_4$ + 0.1 $LiNO_3$ in DOL: DME (1:1)	Soluble LiI gives additional capacity	Chen et al. (2016) Adv. Energy Mater.
Li foil	-	S	KB	0.5w% $LiNO_3$ + 0.5 M LiTFSI in triglyme	GIF cell was introduced	Chen & Hopkins et al. (2016) Energy & Environ. Sci.

KB: Ketjen black

1.3 Yield stress fluids

In the previous sub-chapter, effect of carbon black concentration on mechanical and electrical percolation has discussed. While electrical percolation is favorable for suspension electrode, mechanical percolation may not. Presence of mechanical percolation indicates presence of stress bearing network within the suspension. Such fluids are known as viscoplastic fluids or yield stress fluids.

Yield stress fluids are commonly available around us. Toothpaste, peanut butter, ketchup, lotion and mud are examples of yield stress fluids we see every day. Yield stress stays are solid below at rest and starts flowing above a critical stress. Interactions between microstructures in the fluid gives rise to this behavior. Typically, three main types of microstructure are said to give rise to yield stress behavior: 1) attractive colloids, 2) jammed soft particles, 3) soft glassy hard spheres[36]. Only the first two behavior will be explained here as they are more relevant to the context of this thesis. Microstructure of carbon black particles in the suspension refers to the first type. Attractive forces between carbon black clusters that can be confirmed from zeta potential measurements, helps to create stress bearing percolating network as mentioned in the previous paragraph and as shown in Figure 7. If the percolated network is dense enough (i.e. above percolation threshold), it can give rise to macroscopic elasticity to the system, hence yield stress[36]. Figure 8 shows relationship between yield stress and conductivity of KB in 2.5 M Li-PS in triglyme suspension determined from experiments.

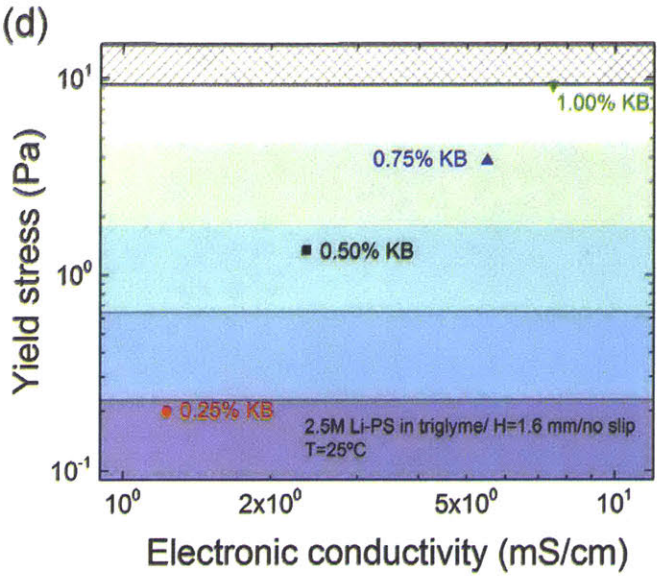

Figure 8: Relationship between yield stress of the KB in 2.5 M Li-PS in triglyme suspension with its conductivity[34]

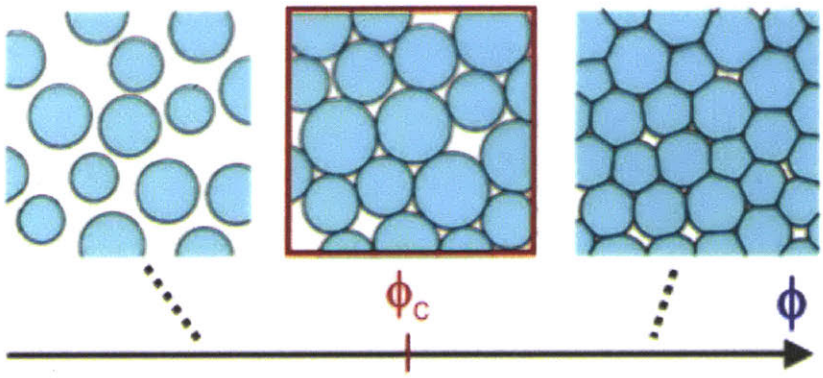

Figure 9: Jamming transition of soft particles[37]

On the other hand, yield stress can also be developed using compressing soft particles against each other as shown in Figure 9. Critical concentration at which this transition occurs is known as jamming transition[36]. Yield stress developed from emulsions and dispersion of microgels (such as Carbopol© and PNIPAM) are due to jamming transition[38]. As will be shown further in detail in

the discussion chapter, both type of microstructure can detrimental and at the same time useful to design suspension electrodes.

Flow behavior of a suspension is usually represented in the form of flow curve. Shear rate $\dot{\gamma}$ [s^{-1}] refers to rate of shear deformation experienced by a fluid element. A flow curve shows amount of stress τ needed to shear a fluid element at a given shear rate. Figure 10 shows flow curve for Newtonian fluid and yield stress fluid For a Newtonian fluid, the shear stress τ [Pa] is directly proportional to the shear rate $\dot{\gamma}$. This relationship is given by the following equation,

$$\tau = \mu\dot{\gamma} \tag{4}$$

where μ [Pa.s] is the dynamic viscosity. However, for yield stress fluid, one has to consider presence of a critical stress at which the fluid starts flowing. Simplest model to describe flow of yield stress fluid is Bingham model. Bingham model is described as

$$\dot{\gamma} = 0 \qquad \text{If } \tau < \tau_y \tag{5}$$

$$\tau = \tau_y + \mu_p\dot{\gamma} \quad \text{If } \tau > \tau_y$$

where τ_y is the yield stress and μ_p is plastic viscosity. In practical fluids, although simple Bingham model does not provide prefect fit with the data, but it is powerful enough to be able to estimate values for engineering applications analytically. For example, pressure drop calculation, determining yield stress, or even crude flow profiles as shown in Figure 11.[39]

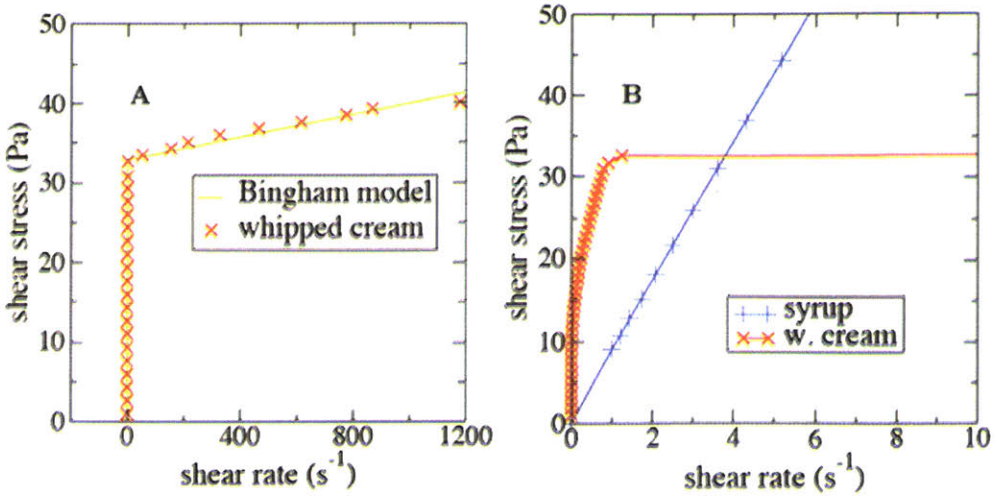

Figure 10: Flow curves for yield stress fluid (left) and Newtonian fluid (right).[36]

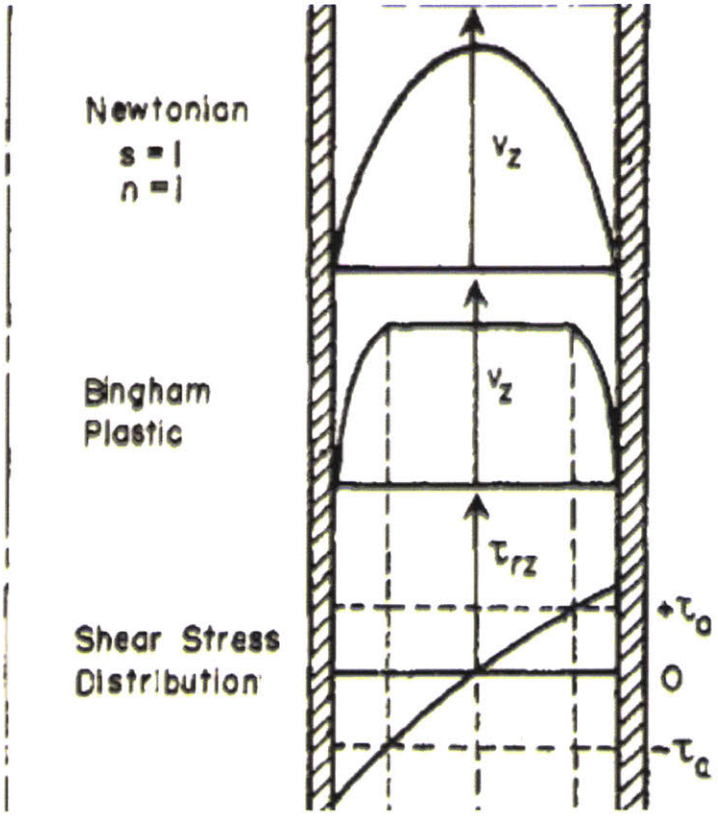

Figure 11: Flow profile for Newtonian fluid and Bingham fluid. At regions where the stress experienced is below the yield stress, the fluid will be unyielded (solid-like)[40]

1.4 Ni-Zn alkaline battery

In this section, a short review will be given on electrodes relevant to this study. Alkaline batteries are one of the earliest commercial batteries. Several battery chemistries have used alkaline electrolyte. For example, Ni-Cd, Ni-Zn, Ni-metal hydride (MH), Ni-Fe, Zn-MnO2 and Zn-air[41]. Excluding its corrosiveness, alkaline electrolyte is inherently more environmentally-friendly because they not flammable and non-volatile compared to organic electrolyte used Li-ion battery. Also, these active materials are also more cheaply and abundantly available compared to cobalt which is commonly used in Li-ion battery[42]. It is also worth to note that early EV used alkaline battery such as Ni-MH before Li-ion batteries.

Suspension electrode is common in alkaline battery such Zn-MnO2 and Zn-air. Figure 12 shows Zn electrode is suspended in gelled electrolyte. It was first introduced by Lewis Urry in 1950s[17]. Redox reaction for Zn electrode is shown in the following equations.

$$ZnO + H_2O + 2OH^- \rightleftharpoons Zn(OH)_4^{2-} \quad (6)$$

$$Zn(OH)_4^{2-} + 2e^- \rightleftharpoons Zn + 4OH^-$$

with reduction potential at -1.2 vs SHE. Zn is oxidized (or ZnO is reduced) through intermediate product zincate ion $Zn(OH)_4^{2-}$. This type of redox reaction is called dissolution and precipitation reaction[43].

Although zinc has high specific capacity among metal electrodes as it gives out 2 electrons and has low discharge voltage, there are several issues in using Zn as rechargeable electrode. One of them is hydrogen evolution. Zinc has lower discharge potential than electrochemical stability window of aqueous solution. In concentrated alkaline solution (pH 14), hydrogen evolution reaction (HER) occurs at ~ 0.83 vs SHE. The redox reaction is given by

$$2H_2O + 2e^- \rightarrow 2OH^- + H_2 \quad (7)$$

This could cause 1) anodic dissolution of Zn to form $Zn(OH)_4^{2-}$ with simultaneous hydrogen evolution and 2) cathodic hydrogen evolution during Zn reduction. These could reduce coulombic efficiency of the battery. One method to prevent hydrogen evolution is to alloy Zn with metals with lower hydrogen evolution overpotential such as Hg, Pb or In[44]. Another problem with rechargeability of Zn is the shape change of the electrode due to migration of soluble $Zn(OH)_4^{2-}$ species[44]. This can be prevented by using additives that can decrease $Zn(OH)_4^{2-}$ solubility in KOH such as $Ca(OH)_2$[45], KF or K_2CO_3[46].

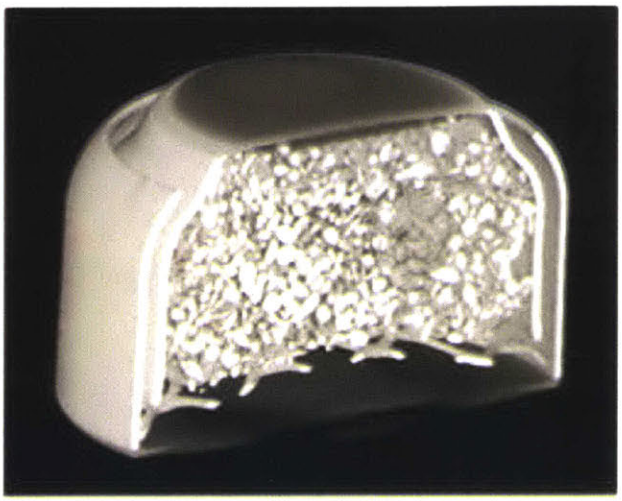

Figure 12: 3D X-ray tomography of Zn suspension in Zn-air button cell.[47]

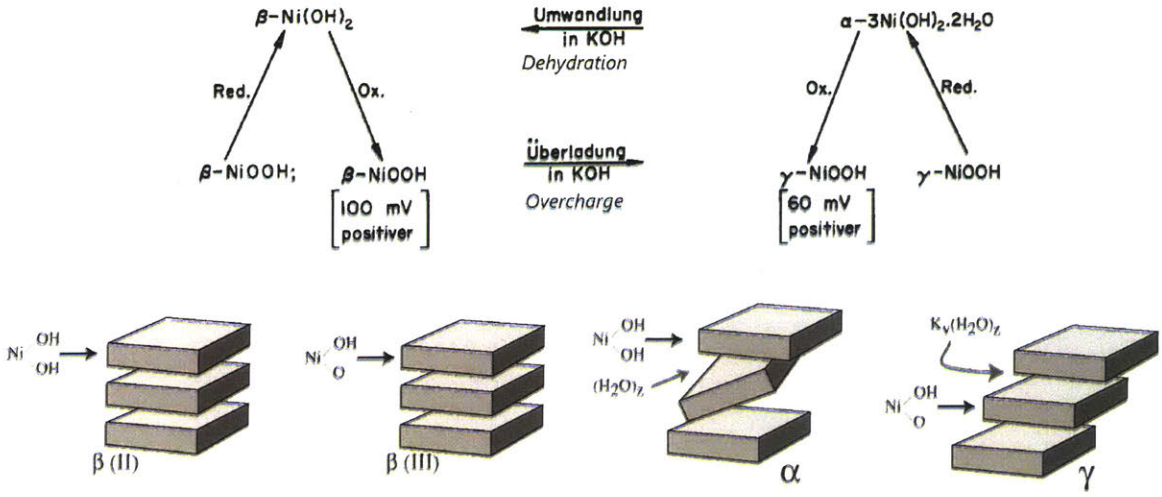

Figure 13: Bode diagram explains structural changes to Ni compound during charge and discharge[48,49]

On the other hand, $Ni(OH)_2$ undergoes proton intercalation and deintercalation during redox reactions. Redox reaction of $Ni(OH)_2$ was found to be complex due to presence of multiple structures and oxidation states of nickel[48,50]. Bode diagram (Figure 13) explains structural changes of nickel compounds during charge and discharge. When β-$Ni(OH)_2$ is charged (oxidized) proton deintercalation happens to form β-NiOOH as shown in the following equation.

$$\beta - Ni(OH)_2 \rightarrow \beta - NiOOH + H^+ + e^- \quad (8)$$

Although layered structure is still maintained (Figure 13), DFT calculations suggests this is a 2-phase reaction, as it involves restructuring of oxygen layer during proton intercalation[49]. When β-NiOOH is overcharged (oxidized further), large energy barrier to remove proton the layered structure causes formation of a more energetically favorable γ-NiOOH (maximum oxidation state +3.66) with intercalation of water and alkali metals from the electrolyte[49]. This has also been observed experimentally[51]. $Ni(OH)_2$ also exists in the form of α-Ni(OH)2. Similar to γ-NiOOH, α-$Ni(OH)_2$ also contains water molecules between the oxygen layers. Hence, oxidation of α-

Ni(OH)2 is assumed to form γ-NiOOH[52]. This has also been observed experimentally, where *in-situ* EQCM of α-Ni(OH)2 during oxidation causes increase in mass which is probably due to incorporation of potassium ions from the electrolyte[53]. When dehydrated under high temperature and concentrated alkaline electrolyte, α-$Ni(OH)_2$ often ages to form β-$Ni(OH)_2$[50,54]. Reversible redox reactions of α/γ and β/β structures are suggested to occur at 0.39 – 0.44 V and 0.44 – 0.47 V vs Hg/HgO respectively[50].

Although there are experimental proofs (as written in previous paragraph) for reversible structural changes of α/γ and β/β structures as suggested by Bode (1966), there have also been several other observations. For example, presence of two plateaus during reduction of Ni compounds at potentials about +0.3 V and 0 to -0.4 V vs Hg/HgO [50,51,54–56]. The origin of reaction at lower potential or more commonly known as second discharge plateau is intriguing because they are not at potentials of reversible α/γ and β/β redox reactions[50,53,57]. Initially there have been suggestions that the presence of second discharge plateau could be due to presence of less active compounds such as $Ni_3O_2(OH)_4$ or $Ni_3O_4.xH_2$, although none of those compounds been observed during electrochemical reduction[51]. Currently, the general consensus is that second plateau could originate from presence of poorly conducting phase within the active material[51,54–56]. This is possible because $Ni(OH)_2$ is an poor electrical conductor[50,51,54–56]. Hence, it was postulated that during discharge, as $Ni(OH)_2$ starts forming till it covers the current collector. Poor conductivity of $Ni(OH)_2$ causes ohmic drop, hence lower discharge plateau[54,55,58]. This could also be related to positive correlation observed between relative amount of γ-NiOOH in the sample and relative capacity from the second discharge plateau[56] because of overcharge during oxidation of Ni(OH)2 only near the current collector. Some studies have suggested coating the Ni(OH)2 particle with CoO could prevent the observation of second discharge plateau due its high electrical

conductivity[55]. Nevertheless, these observations point the importance of understanding the coverage of $Ni(OH)_2$ with conductive particle.

Generally, Ni(OH)2 has good rechargeability. However, high oxidation potential of $Ni(OH)_2$ ~0.47 V vs Hg/HgO is higher than the thermodynamic potential for oxygen evolution. Oxygen evolution reaction as shown in the following equation occurs at ~ 0.3 V vs Hg/HgO at pH 14.

$$O_2 + H_2O + 4e^- \rightarrow 4OH^- \quad (9)$$

This could result in low coulombic efficiency and drying of the electrolyte.

1.5 Scope of study

1.5.1 Objective of this study

This study aims to find an appropriate framework to design high performing suspension for semi-solid flow battery. High performing suspension is defined as suspension with high energy density to minimize volume of the tank, suspension with high power density to minimize area of stack, suspension with high stability to prevent sedimentation and suspension with good flowability to minimize energy loss due to pumping. Tools to test the properties of the suspension relevant to above performance parameters will be developed or adapted to meet the requirements of concentrated alkaline electrolyte. A flow cell will then be designed and fabricated to test the performance of the suspension in an open cell system as a first step to device SSFB.

1.5.2 Choice of battery chemistry

Most studies till now have focused on Li-ion or Li-S battery chemistries (Table 1). Considering alkaline electrolyte is more environmentally-friendly, Zn-Ni battery chemistry is chosen. Zn-Ni battery has one the highest potential for aqueous battery. For suspension with 40 vol% Ni(OH)2 active material particles, the molarity could reach up to ~17.7 M. This is about 7 times larger than maximum solubility of VOSO4 in water.

Although there has been prior report by Liu and Wang (2015) on Zn-Ni SSFB, they have reported several problems such phase separation of the suspension, which then affected electrochemical performance of the battery[59]. Hence, this highlights the importance of fundamental understanding of how to design a high performing SSFB suspension.

1.5.3 Stability, conductivity and flowability

Sections 1.2 and 1.3 show the complexity in designing suspension electrode for semi-solid flow battery. Suspension composition affects suspension properties, suspension properties affect suspension and system performances (Figure 14). Here, suspension performance is defined as performance that can be evaluated without knowledge of the opposite suspension electrode (i.e. with reference electrode). This shows that knowledge required to design a suspension with high performing suspension (*i.e.* high energy density and power density capabilities, minimum energy loss due to pumping, while maintaining stability over long period of time) are interdisciplinary. Systematic approach has to be taken to design these suspensions can serve as a model framework to design high-performing suspension for any battery chemistries.

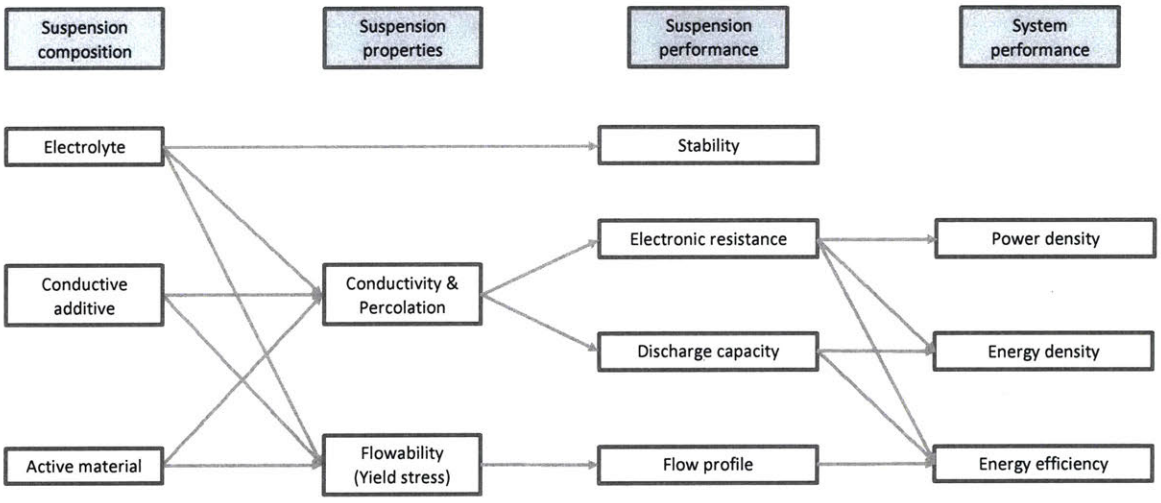

Figure 14: Relationship chart between suspension components, suspension properties, suspension performance and system performance. This relationship is just summary based on literature review done in sections 1.2 and 1.3. Obvious relationship such as choice of active material affecting the suspension and system performance is not shown here.

Only three main suspension properties will be focused in this study: stability, conductivity and flowability. Firstly, high stability of the suspension can extend cycle life of the suspension. Secondly, suffice conductivity and good electrical percolation can ensure minimum internal resistance of the battery and also improve the discharge capacity of the battery. Thirdly, finding the flowability of the suspension (*i.e.* yield stress) can help to estimate energy loss due to pumping such solid-like gels.

2. Experimental procedures

2.1 Materials

Potassium hydroxide (KOH, 99%, VRM) was used for electrolyte preparation. Carbopol© (Carbopol© 940 NF polymer, Lubrizol, USA) was used as gelling agent. Zinc oxide (ZnO, 99%, Sigma-Aldrich) and alloyed zinc powder (EverZinc, Belgium) were used for anolyte preparation, where Zn served as conductive additive. Nickel hydroxide ($Ni(OH)_2$, 98%, Pred Materials, USA and Kansai Catalyst Co. Ltd., Japan) and carbon black (acetylene black, Chevron, USA) were used for catholyte preparation, where carbon black served as condutive additive. Cobalt oxide (CoO, 99.995%, Fisher Scientific) was as conductive additive to further enhance conductivity of Ni(OH)2 as suggested by Leger et al (1999).[55]

2.2 Preparation of suspensions

2.2.1 Catholyte preparations

30 w% KOH solution (7 M KOH solution) was prepared by dissolving 5.36 g of KOH pellets in 12.5 ml deionized water. Then, 0.18 g of Carbopol© was added to above solution and mixed with planetary mixer. The electrolyte gel was kept at rest for 12 hours to allow swelling of Carbopol© microgels. The electrolyte gel was then remixed before adding carbon black at amounts as described in the text, and mixed again after. For preparation of active suspension, Ni(OH)2 + CoO (100 : 5 by weight) powder mixture was ground with carbon black prior to adding to electrolyte gel at Ni(OH)2 amounts described in the text. All mixing was performed at 2000 rpm for 12 minutes. Composition of the suspension in the text is described in w% with respect to water. For example, composition in w/w_{water}% carbon black : $Ni(OH)_2$: Carbopol© = 14.0 : 39.8 : 1.4, would mean 2.03 g of carbon black, 8.26 g of Ni(OH)2 and 0.18 g of Carbopol©.

2.2.2 Anolyte preparations

30 w% KOH solution (7 M KOH solution) was prepared by dissolving 5.36 g of KOH pellets in 12.5 ml deionized water. Then, 0.57 g of ZnO was added to above solution and stirred using magnetic stirrer for 5 hours to saturate the solution with zincate ions. After that, 0.18 g of Carbopol© was added to above solution and mixed with planetary mixer. The electrolyte gel was kept at rest for 12 hours to allow swelling of Carbopol© microgels. The electrolyte gel was then remixed before adding ZnO at amounts as described in the text, and mixed again after. Finally, Zn was added to the suspension and mixed at 2000 rpm for 6 minutes. All other mixing was performed at 2000 rpm and 12 minutes unless stated otherwise. Composition of the suspension in the text is described in w% with respect to water. For example, composition in w/w_{water}% Zn : ZnO : Carbopol© = 71.1 : 42.1 : 1.8, would mean 9.12 g of ZnO, 30.8 g of Zn and 0.23 g of Carbopol©.

2.3 Electrochemical measurements

2.3.1 Conductivity measurements

Conductivity of the suspensions were measured using in-house conductivity cells. The suspensions were filled in rubber gasket separated by two blocking electrodes. For catholyte, impervious graphite plates (Fuel Cell Store, USA) were used as electrode. For anolyte, brass plates (McMaster, USA) were used as electrode. The geometrical area was 0.79 cm^2 and thickness of the gasket was 0.17 cm for both cells. Resistance of the suspension was determined by sweeping potential across the electrode as described in the text. Conductivity was calculated based on following equation.

$$\sigma_e = \frac{1}{R}\left(\frac{t}{A}\right) \tag{10}$$

where t is the thickness of the gasket and A is the geometrical area of the cell.

2.3.2 Electrochemical performance of suspension in static closed cell

To determine intrinsic electrochemical performance of the suspension, the active suspensions were charged and discharged in a closed cell and static mode. This is important because it has been shown that, in an open cell, electroactive zone extension can occur due to conductive nature of the suspension[60]. Design of the suspension cell is shown in Figure 15. Depth of the graphite well for catholyte and thickness rubber gasket for anolyte was 2 mm and 1.7 mm. Effective geometrical area the suspensions were 1.11 cm^2. Charge-discharge were performed as described in the text. The discharge capacity will gradual increase with cycle as result of transition from α/γ and β/β redox reactions in positive electrode.[53] Hence, only the cycle with highest capacity is reported here (~3rd cycle).

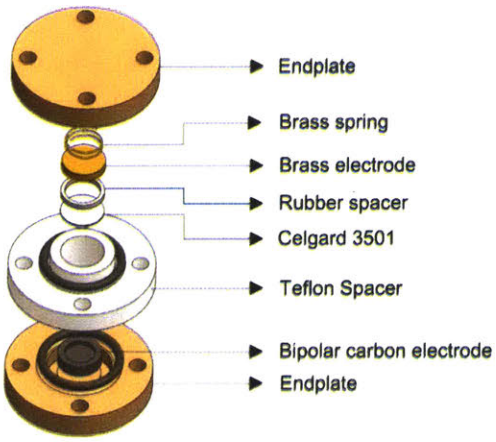

Figure 15: Static closed cell used to determine intrinsic electrochemical performance of the suspensions

2.4 Rheological measurements

Rheological measurements of the suspensions were performed on AR-G2 rheometer (TA Instruments) using 40 mm plate-plate geometry. To prevent wall slip[36] and avoid contact of the suspension with the stainless steel rheometer plates, the plates were covered with adhesive-back lapping film with 30 μm diamond abrasive (3M Corp.) for catholyte suspension and adhesive-back sandpaper with 100 μm silicon carbide abrasive (McMaster-Carr, USA) for anolyte suspension. The abrasive particle sizes were chosen to match the average size of Ni(OH)2 and Zn particles respectively. 1200 μm gap was used for all measurements unless stated otherwise. Decreasing step shear rate controlled viscometry was performed to measure the flow curve. Each shear rate was held constant for 30 s before measuring the stress. Same procedure was repeated three times with fresh samples to obtain average stress at a given shear rate.

3. Results and discussion

3.1 Developing yield stress in continuous medium to design stable suspension

Figure 16 shows pictures of stable and unstable suspensions in 7 M KOH electrolyte with and without addition of polymer-based microgel (Carbopol©) respectively. Unlike carbon and active material suspensions in organic electrolytes used in the literature, these particles do not readily suspend in the electrolyte[14,29]. Difference in stabilization mechanism is described as follows.

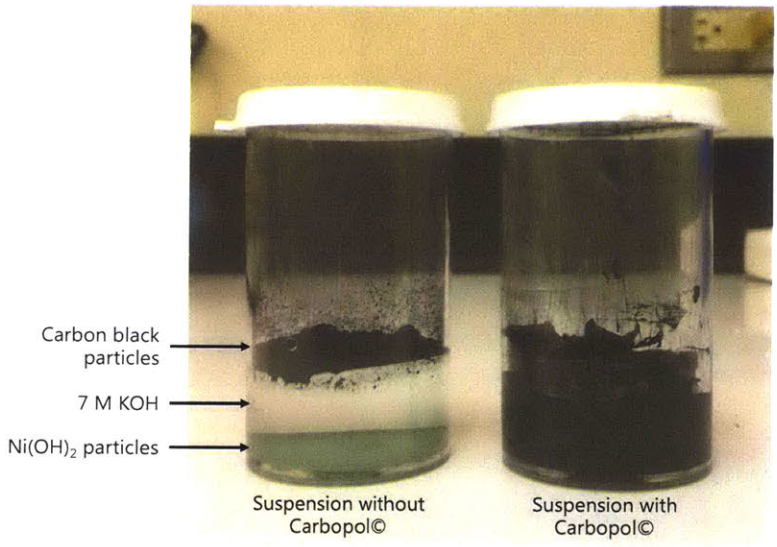

Figure 16: Photographs of stable and unstable catholyte suspension. Suspensions are stabilized by adding Carbopol©, which creates stress-bearing microgel structures in the electrolyte. Composition of suspension on the right is (in $w/w_{water}\%$) carbon black : $Ni(OH)_2$: Carbopol© = 14.0 : 39.8 : 1.4).

Generally, two types of dominating body forces determine if particles will undergo sedimentation: gravitational force (scales as $F_G = a^3 \Delta\rho g$) and Brownian force (scales as $F_B = k_B T/a$), where a is the particle size and $\Delta\rho$ is the density difference between the particle and the

continuous phase (electrolyte) [61]. When Brownian force is dominant, these particles are usually referred as colloids and they also experience interparticle colloidal forces such as attraction or repulsion due to their surface charge [62]. Here, it is worth noting that surface charge is dependent on the functional groups on the surface of the particle, type of solvent and salt concentration. If F_G/F_B is more than unity, the particles tend to undergo sedimentation. The particle size magnitude limit for dominant Brownian and colloidal force is about ~1 μm. Figure 17 shows SEM images of particles used to compose the catholyte and anolyte suspensions used in this study. Hence, one can expect carbon particles (~100 nm) to be dominated by Brownian and colloidal forces, and Zn (~100 μm), ZnO (~30 μm), $Ni(OH)_2$ (~12 μm), LFP (~4 μm) [29], LCO (~3 μm) [14], LTO (~3 μm) [14] by gravitational force.

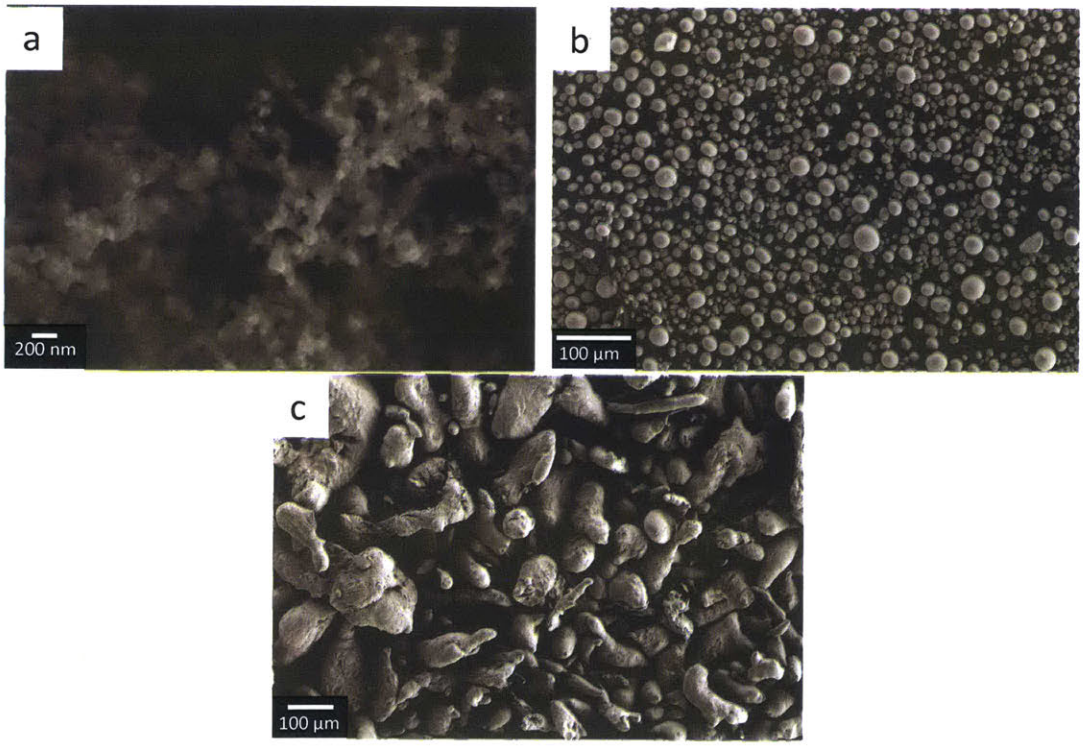

Figure 17: SEM images of particles required to make composition of catholyte and anolyte used in this study

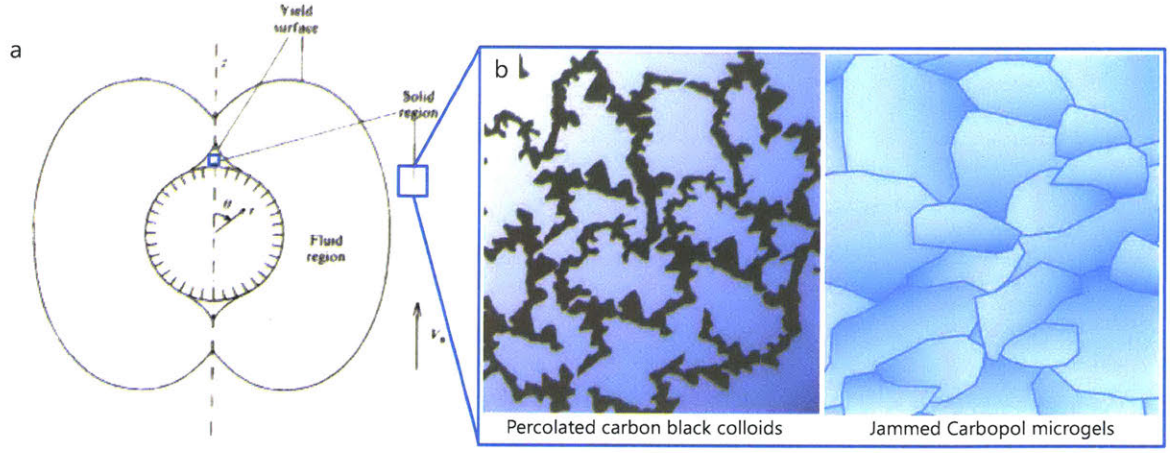

Figure 18: a) Schematic of fluid and solid region around sphere suspended in continuous medium filled with stress-bearing network (yield stress fluid) (figure from [63]); b) Schematic of stress-bearing network made up of percolated carbon black colloids (left) and jammed Carbopol microgels (right). Carbon black colloid exists as fractal like network in suspension [27] and Carbopol microgels exists as swollen sponge [64]

In order to suspend these "large" particles that are dominated by gravitational force, a stress bearing continuous medium is needed [63]. As discussed in the introduction, this stress bearing continuous medium, or yield stress fluid, is a fluid that starts above a critical stress and stays solid below the critical stress. The presence of critical stress is due to presence of stress bearing microstructures within the continuous medium [65]. Figure 18 shows predicted shape of fluid and solid regions when a spherical particle is placed in an ideal yield stress fluid (also known as Bingham fluid) [63]. As shown in Equation 11, whether or not if the yield stress of the continuous medium is enough to suspend the particle, is dependent on the non-dimensional yield stress parameter Y_g [66].

$$Y_g = \frac{3\tau_y}{\Delta\rho g a} \tag{11}$$

Here, τ_y is yield stress of the continuous medium, $\Delta\rho$ is the density difference between continuous medium and the sphere, a is the diameter of the sphere. This parameter is the ratio of reaction force from yield stress of the continuous medium ($\pi a^2 \tau_y/2$) and gravitational force ($\pi a^3 \Delta\rho g/6$). If the continuous medium is ideal Bingham fluid, as $Y_g \rightarrow Y_{g,crit} = 0.14$, the fluid region shrinks, and $Y_g \rightarrow 0$ (Stokes flow in Newtonian continuous medium), the fluid region grows infinitely [63]. However, unlike ideal Bingham fluid where the yield stress where the yield stress homogeneous throughout the continuous medium and is independent on the microstructure that causes the yield stress, in a practical scenario, the yield stress will depend on microstructure in the yield stress fluid [66]. For example, $Y_{g,crit} = \sim 0.3$ for neutralized Carbopol© microgel and ~ 0.05 for cellulose fiber colloidal [66].

As shown in Figure 18, when the "large" active material particles is dispersed in organic electrolyte, colloidal forces due to charge adsorption [21] on the surface of hydrophobic carbon black particles helps to create a percolated mechanical network within the suspension. This network develops yield stress within the continuous phase, which is enough to "trap" larger active material particle preventing sedimentation as discussed above. Hence, in this case, the carbon black particles work as both conductive additive and also as suspension stabilizing agent.

On the other hand, in 7 M KOH aqueous electrolyte used in this study, since hydrophobicity of carbon black surface prevents dispersion and formation of percolated network by the particle, stable suspension cannot be achieved. Traditionally, as demonstrated by Parant et al. (2017), early calligraphists added polysaccharide-based polymer such as gum Arabic to the aqueous solvent to functionalize carbon black surface and stabilize the ink suspension [27]. However, such technique may not work for this instance as polysaccharides undergo hydrolysis in concentrated alkaline environment[67]. Therefore, we introduce polymer-based microgel (Carbopol©) structure in the

electrolyte to "trap" both carbon particles and Ni(OH)2 for cathoyte, Zn and ZnO for anolyte. Similar technique has been used to stabilize Zn suspension in commercial alkaline primary battery.[68]

Microgel refers to intramolecularly cross-linked polymer swollen in the solvent. At high concentrations, microgels form a jammed, continuous and elastic network [69]. This method is commonly used in complex formulations of food and pharmaceutical products. We have used commercially available poly(acrylic) acid-based Carbopol© in this study. In neutral pH, Carbopol© undergoes jamming transition at about ~ 0.1 $w/w_{water}\%$ [70]. We have used 1.4 $w/w_{water}\%$ and 1.8 $w/w_{water}\%$ for catholyte and anolyte respectively. As shown in Figure 19, the electrolyte gel had yield stress of 0.7 Pa and 7 Pa, suffice to suspend largest particle in the composition from Equation 11. Stability of both catholyte and anolyte is evident from tomography measurements shown in Figure 20.

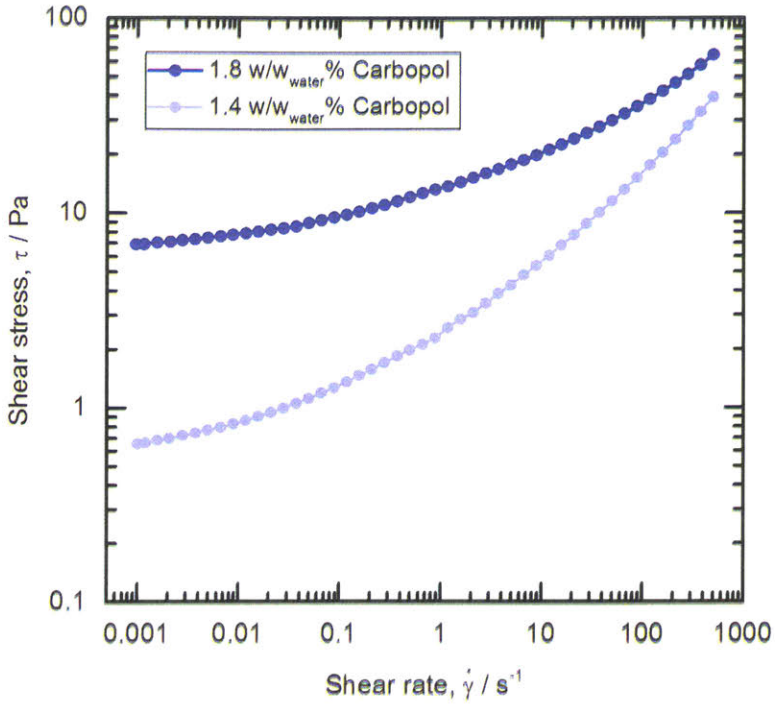

Figure 19: Flow curve of Carbopol only suspensions in 7 M KOH which are used as suspending medium for catholyte (1.4 w%/w_{water}% Carbopol) and anolyte (1.8 w%/w_{water}% Carbopol). The yield stress is 0.7 Pa and 7 Pa respectively.

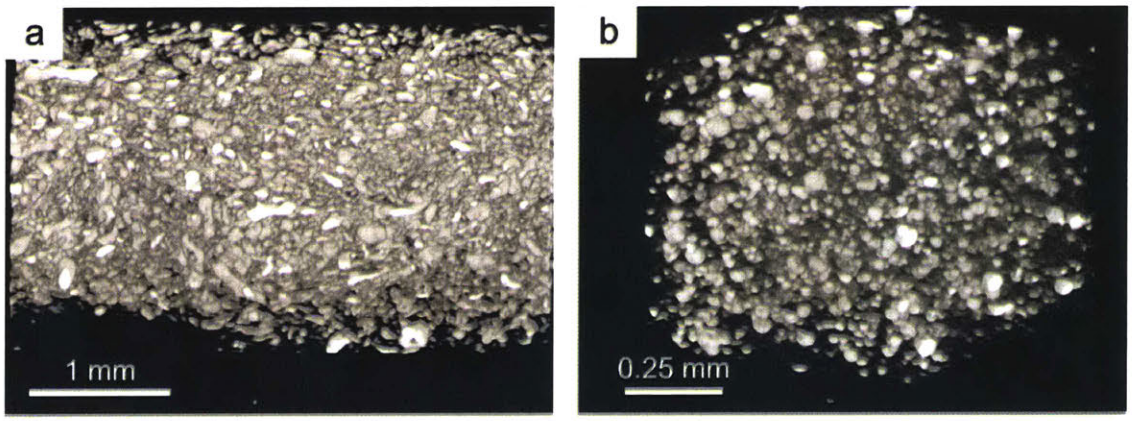

Figure 20 3-D tomography of anolyte (composition in w/w_{water}% Zn : ZnO : Carbopol© = 71.1 : 42.1 : 1.8) and catholyte (composition in w/w_{water}% carbon black : $Ni(OH)_2$: Carbopol© = 14.0 : 39.8 : 1.4) measured using X-ray CT-scan. Samples were measured over a month after preparation

3.2 Percolation of conductive additive and its effect on electrochemical performance

Conductive additive creates space-spanning network within the suspension. This network behaves like flexible wire that bridges the current collector and the active material [71]. The cluster size of the space spanning network grows with concentration of the conductive additive and reaches an infinitely large size at the percolation threshold ϕ_c [24,72]. Determination of percolation threshold of conductive additive is important to ensure there is continuous pathway for electron conduction. There are two commonly used methods to find percolation of conductive additive, by measuring elastic modulus G_0' of the suspension or by measuring conductivity σ_e of the suspension [73,74]. As shown in equation 12 and 13, both properties show power-law increase above the percolation threshold. Here, ν and s are rigidity percolation index and conductivity percolation index respectively [32]

$$G_0' \sim (\phi - \phi_c)^{\nu} \tag{12}$$

$$\sigma_e \sim (\phi - \phi_c)^{s} \tag{13}$$

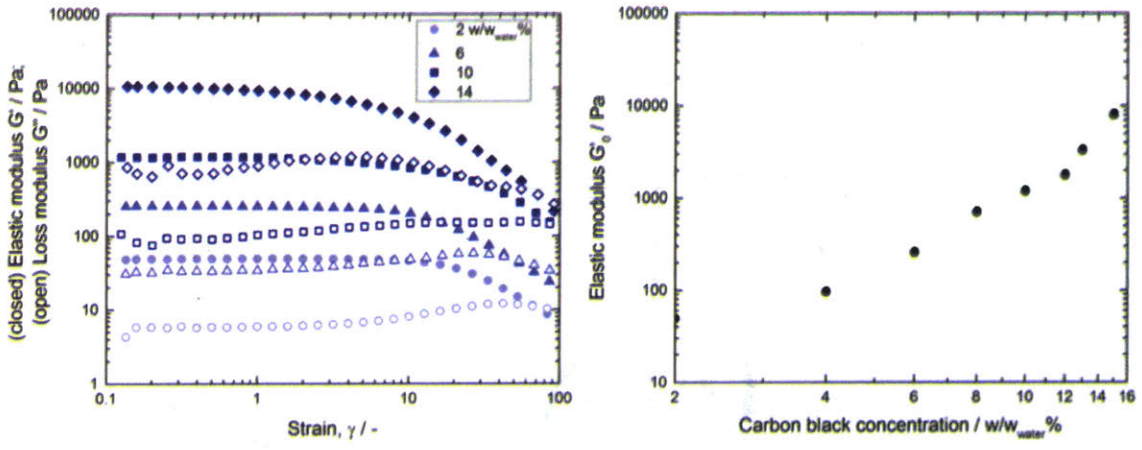

Figure 21: (left) Linear viscoelastic (LVE) region is determined from storage modulus vs strain measured under 1 Hz oscillation at gaps between 1300 to 1400 micron. (right) Elastic modulus in LVE region for carbon black suspension with different concentration of carbon black in 1.4 w/w_{water}% Carbopol + 7 M KOH.

Figure 21 shows elastic modulus measured for different concentration of carbon black in 1.4 w/w_{water}% Carbopol + 7 M KOH. There is no obvious sharp increase in elastic modulus with different concentration of carbon black, due to the contribution of elasticity from continuous medium itself. Hence, conductivity method was used to determine the percolation threshold as there will be no contribution from the continuous medium.

Figure 22 shows electronic conductivity of suspensions at different amount of carbon black for catholyte and Zn for anolyte. Percolation threshold is about 6 w/w_{water}% (~3 v/v_{total}%) for carbon black and 48 w/w_{water}% (~10.5 v/v_{total}%) for Zn. These numbers are much lower than theoretical percolation threshold for spherical particle which is 28 v/v_{total}% [75].This deviation can be explained from fractal like shape of carbon particles and highly anisometric shape of Zn particles shown in Figure 17. It is worth to note that conductivity of the conductive suspension is still nearly maintained upon addition of high amount of active material: 4.12 ± 1.09 mS/cm for carbon black + $Ni(OH)_2$ suspension (composition in w/w_{water}% carbon black : $Ni(OH)_2$: Carbopol© = 14.0 : 39.8 : 1.4) and 67 ± 7 mS/cm for Zn + ZnO suspension(composition in w/w_{water}% Zn : ZnO : Carbopol© = 71.1 : 42.1 : 1.8). This suggests that theoretically we will be able to achieve catholyte with 5.4 M active material concentration and energy density of 240 $Wh/L_{catholyte}$ (~6 times of catholyte for vanadium flow battery). Also, having high conductivity allows one to use thick electrode channels that could minimize pumping loss [29].

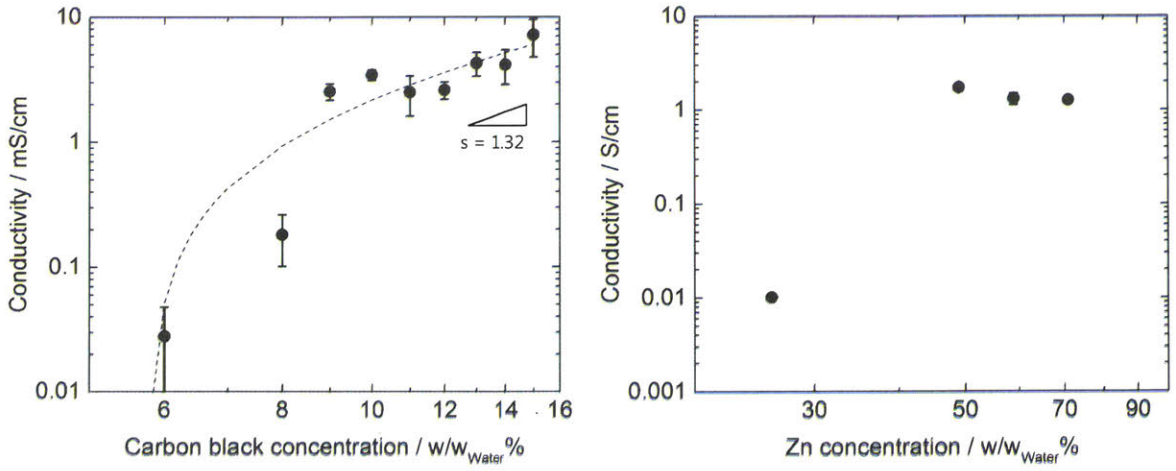

Figure 22: Conductivity of suspensions with different amount of conductive additive a) carbon for catholyte (in mS/cm) and b) Zn for anolyte (in S/cm). Conductivity percolation threshold is about 6 w/w$_{water}$% carbon and 49.8 w/w$_{water}$% Zn respectively. Conductivity was calculated from linear scan voltammetry technique. The scan rate is 0.1 mV/s. The voltage range is 0 to 30 mV for carbon suspension and 0 to 10 mV for Zn suspension.

Now, since we know the percolation threshold of conductive additive for both suspensions, we then proceeded to understand effect of carbon concentration on electrochemical behavior of $Ni(OH)_2$ in conductive suspensions. To ensure ohmic resistance or percolation of conductive additive of the anolyte is not performance limiting factor in these experiments, here onwards, we have used 71.1 w/w$_{water}$% Zn as conductive additive for all future experiments. Figure 23 shows charge discharge curves for same composition of $Ni(OH)_2$ (3 w/w$_{water}$%) with different concentrations of carbon black (6 to 14 w/w w/w$_{water}$%) taken in a static closed cell. X-axis is shown as normalized capacity, which refers to capacity normalized to charge capacity. As one can observe, the charging potential (~2 V vs $Zn/Zn(OH)_4^{2-}$) seems to be similar for all concentrations of carbon black indicating that ohmic drop due to lower conductivity for lower concentration of carbon black is not really are big contributing factor for the trend during discharge. Two discharge

plateaus are observed during discharge: 1) till 1.1 V and 2) between 1.1 and 0.8 V, indicating two different phase transformations [76]. As shown in Figure 24, the discharge capacity of the first plateau increases, and capacity of the second plateau decreases with concentration of carbon black. The overall normalized discharge capacity reached a maximum value at ~ 0.8.

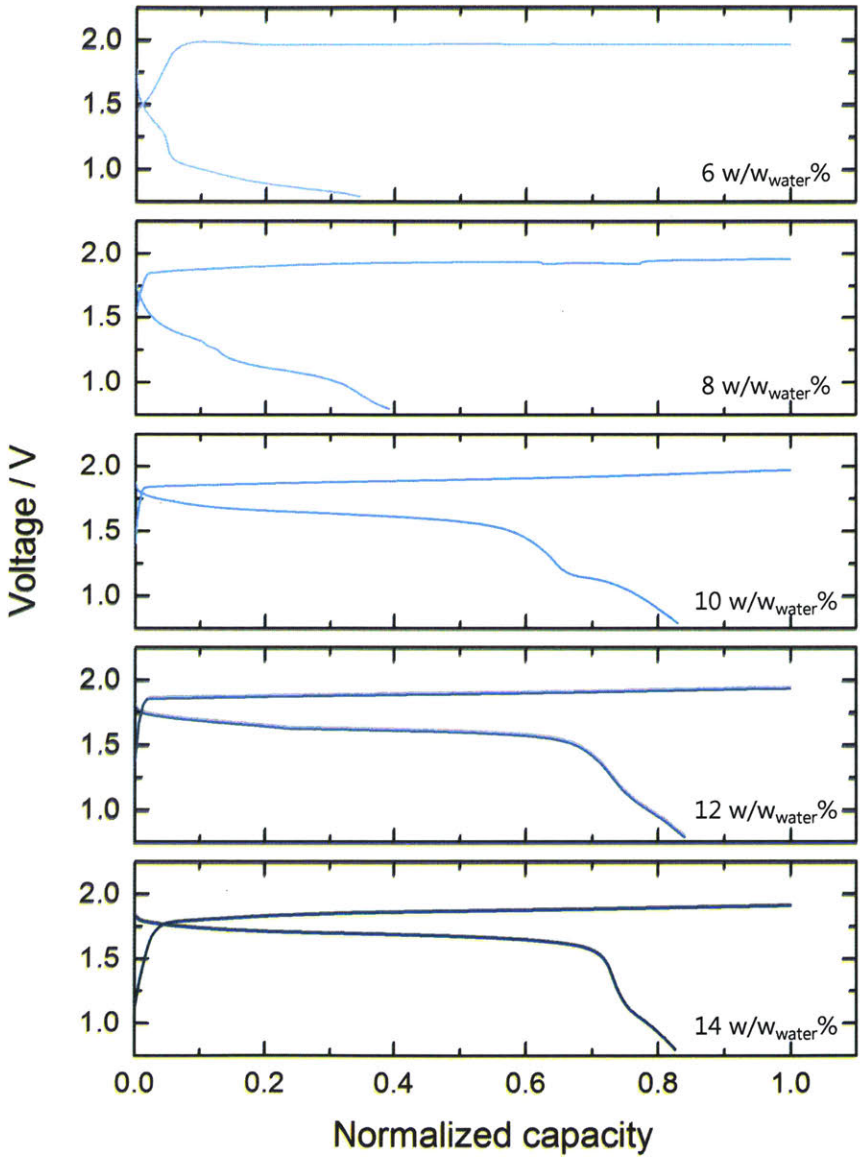

Figure 23: Galvanostatic (2.0 mA/cm^2) charge-discharge curves for catholyte with different carbon concentrations (composition in w/w$_{water}$% carbon black : $Ni(OH)_2$: Carbopol© = 6 to 14 : 3 : 1.4)

in static closed cell. Anolyte composition (in w/w_{water}% Zn : ZnO : Carbopol© = 71.1 : 21.4 or 31.3 : 1.8) was fixed at Zn concentration above percolation threshold to minimize ohmic polarization. All samples were charged to 80% SOC of Ni(OH)2 and discharged to cut-off potential of 0.8 V. X-axis refers to capacity normalized to charge capacity. (Data for 10, 12, 14 w/w_{water}% carbon black courtesy of Yunguang Zhu)

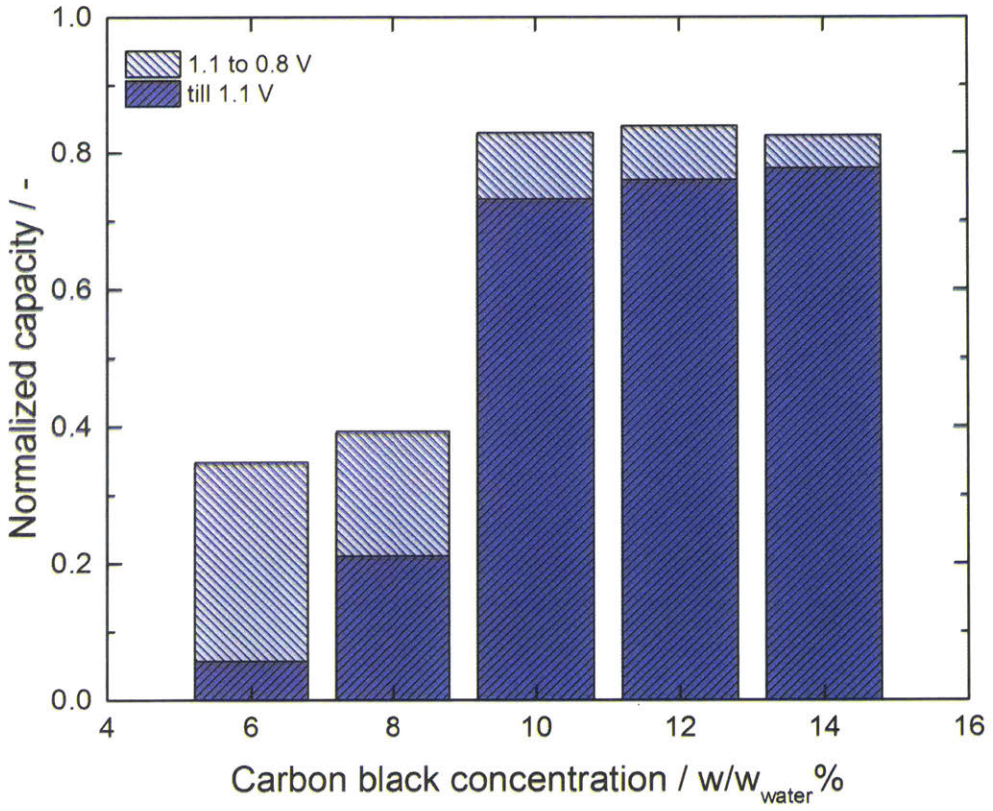

Figure 24: Faradaic efficiency for catholytes from Figure 23 in static closed cell. Two different discharge plateaus refers to two different discharge regimes: 1) till 1.1 V and 2) between 1.1 to 0.8 V[76]. Y-axis refers to capacity normalized to charge capacity (Couloumbic efficiency).

Observations from conductivity of suspensions in Figure 22 can be used to explain the trend in discharge capacity. At percolation threshold, since there is an infinitely connected network, some discharge capacity can be obtained from $Ni(OH)_2$ particles at the vicinity of carbon black network. As the size the carbon black percolated network increases, more $Ni(OH)_2$ particles can be accessed, hence increase in discharge capacity. When carbon black concentration is well above percolation threshold $\sigma_e \sim \phi^s$, the amount of $Ni(OH)_2$ particles can be accessed by the carbon black network is now limited by the Ni(OH)2 in the suspension, hence, similar ~ 80% coulombic efficiency above 10 w/w_{water}% carbon black. Similar observation was found by Franco et al. from their kinetic Monte Carlo studies [77]. However, they have postulated that some capacity can observed even below percolation threshold and discharge capacity is invariant of conductive additive concentration above percolation threshold. Our study suggests that even above percolation threshold, the conductive additive concentration should reach the $\sigma_e \sim \phi^s$ regime before discharge capacity reaches maximum. This difference in observations could be due to small model size used [78]or over-contribution of particle Brownian diffusion [74] in their study by Franco et al. Both reasons can affect percolation behavior or particles in a system.

The difference in ratio of capacity obtained from two discharge plateaus, can be explained from explanations given by Delmas et al. [76] in Figure 25. During beginning of discharge, better ionic and electronic conductivity of β- $NiOOH_{1.25}$ due to its presence of proton vacancies, allows intercalation of proton at various points in the particle. When the contact with the conductive region is covered by a certain concentration of insulating $NiOOH_{2-\varepsilon}$, the ohmic resistance may increase to discharge the remaining $NiOOH_{2-\delta}$ [76], leading to formation of second plateau. This is a plausible explanation because when the carbon black concentration increases, the void between percolating network becomes smaller and leads to better coverage of conductive additive around

$Ni(OH)_2$. Hence, the ratio of capacity from second discharge plateau gets smaller with increasing amount of carbon black. We also would like to note that the presence of second discharge plateau could also have some contributions from discharge of γ - NiOOH or oxygen reduction[56,58]. Nevertheless, explanation from Delmas et al. and observations from Figure 23 and Figure 24 are suffice to highlight the effect of conductive percolation on electrochemical performance of semi-solid battery.

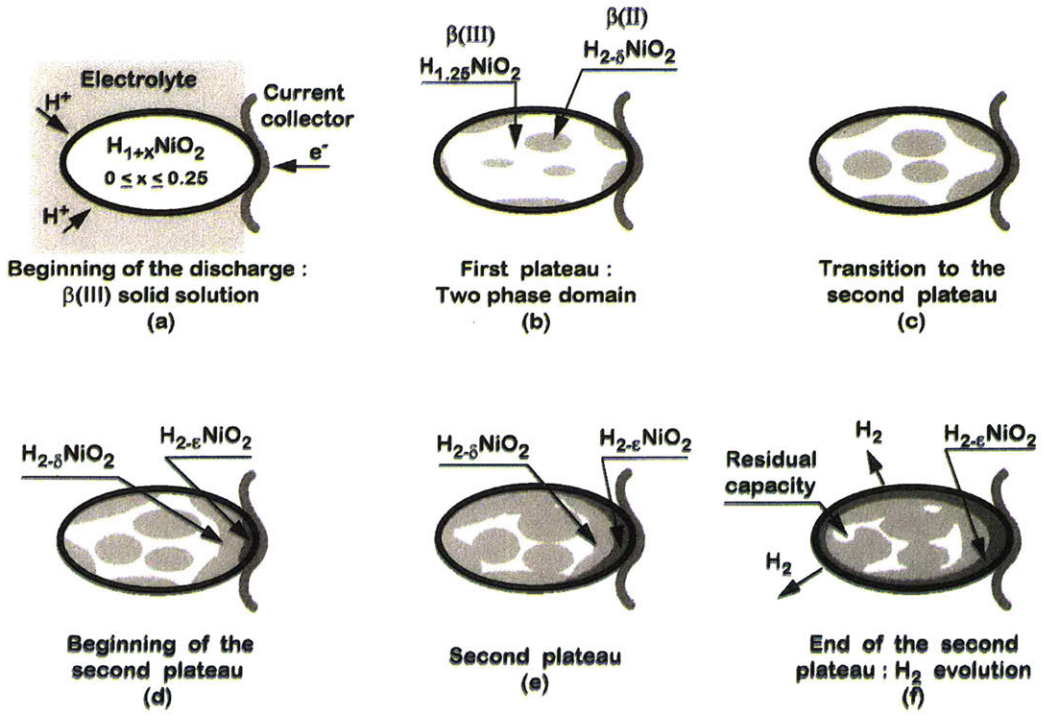

Figure 25: Proposed mechanism on how poor connectivity between Ni(OH)2 and current collector can cause occurrence of second plateau in Ni(OH)2 electrode by Delmas et al. [76]

3.3 Semi-solid battery in static closed cell with high energy and power densities

Since now we know the optimum concentration of conductive additive (14 w/w_{water}% carbon black for catholyte), we then proceeded to prepare and test catholyte and anolyte with high energy density at different current densities. All these experiments were still done in static closed cell to simplify the electrochemical charge-discharge process and understand the intrinsic electrochemical performance of these suspensions. Figure 26 shows galvanostatic charge-discharge curves at various current densities in static closed cell with 39.8 in w/w_{water}% Ni(OH)2 catholyte. Energy density of catholyte $E_{catholyte}$ used in x-axis was calculated using Equation 14. where volume refers to volume of the catholyte used (0.22 cm^3).

$$E_{catholyte} = \frac{\int V\, dQ}{\text{Vol.}} \tag{14}$$

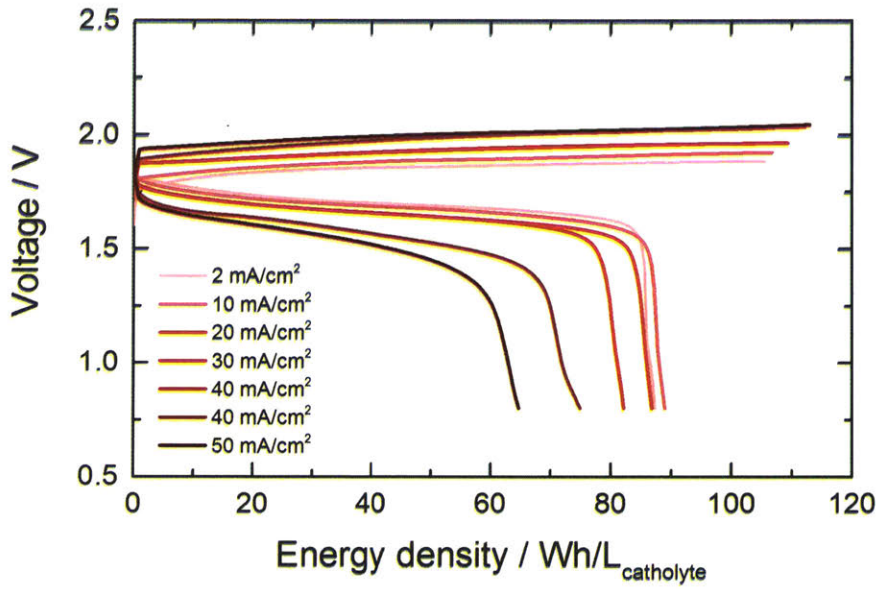

Figure 26: Galvanostatic charge-discharge curves at various current densities in static closed cell. Catholyte composition (in w/w_{water}% carbon black : $Ni(OH)_2$: Carbopol© = 14 : 39.8 : 1.4). Anolyte composition (in w/w_{water}% Zn : ZnO : Carbopol© = 71.1 : 31.3 : 1.8). All samples were

charged to 40% SOC of Ni(OH)2 and discharged to cut-off potential of 0.8 V. Energy density was obtained by integrating voltage profile with respect to capacity and dividing with volume of catholyte used (0.22 cm^3). (Courtesy of Yunguang Zhu)

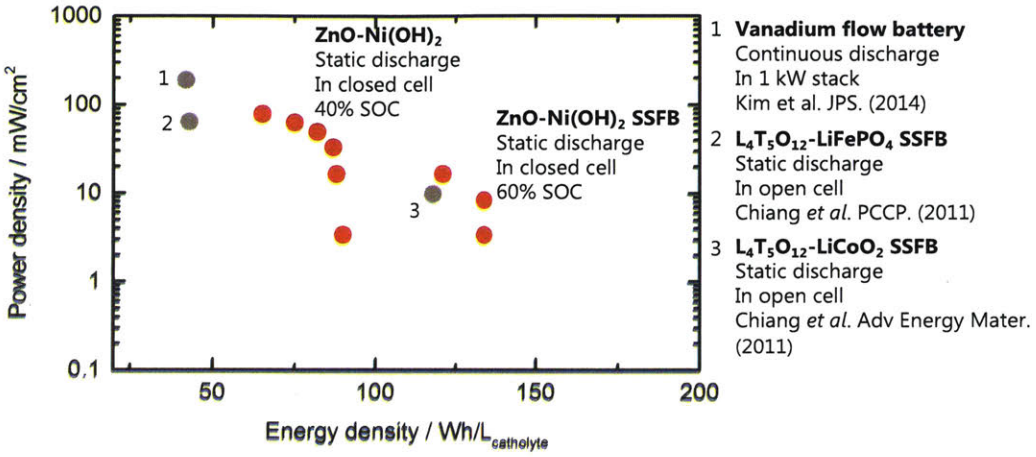

Figure 27: Modified Ragone plot to compare performance of other static semi-solid battery and VRFB reported in literature on modified Ragone plot. Higher power density on Y-axis minimizes stack cost, and higher energy density on X-axis minimizes battery suspension tank size. Catholyte composition (in w/w_{water}% carbon black : $Ni(OH)_2$: Carbopol© = 14 : 39.8 : 1.4). Anolyte composition (in w/w_{water}% Zn : ZnO : Carbopol© = 71.1 : 31.3 : 1.8). Only systems with flowable electrode for anolyte and catholyte is compared.

Figure 27 shows modified Ragone plot to compare the performances of other semi-solid flow systems reported in literature. Power density $P_{density}$ in Y-axis is calculated using Equation 15. Here t refers to time taken to discharge the battery and A is geometrical reaction area.

$$P_{density} = \frac{\frac{\int V\, dQ}{t}}{A} \tag{15}$$

Ragone plot is commonly used to interdependence of energy output and power output of a battery system. Using Ragone plot to compare flow battery systems is not desirable because flow battery decouples power and energy output. Common parameters that determines applicability of flow battery is cost of the battery stack and size of the system. Hence, we use power density as a parameter that evaluates cost of battery stack and energy density as a parameter that evaluates size of a system. As shown in Figure 27, performance of catholyte (in $w/w_{water}\%$ carbon black : $Ni(OH)_2$: Carbopol© = 14 : 39.8 : 1.4) designed in this study, exceeds energy density and power density of other semi-solid static systems reported in the literature. Also, maximum energy density obtained is ~ 3 times of energy density of VRFB. This is a desirable output for large-scale energy storage systems.

3.4 Flowability of catholyte and anolyte

3.4.1 Flow curves for catholyte and anolyte

Flow curves of suspensions with highest concentration of active material, catholyte composition (in w/w_{water}% carbon black : $Ni(OH)_2$: Carbopol© = 14 : 39.8 : 1.4); anolyte composition (in w/w_{water}% Zn : ZnO : Carbopol© = 71.1 : 31.3 : 1.8) in Figure 28 and Figure 29. As expected both suspension exhibited non-Newtonian properties such as shear thinning and presence of yield stress. For catholyte suspension, discontinuous drop in shear stress was observed at about 45 s^{-1}. This observation could be due to experimental artefact such as slip [69]. Since our goal to find an estimate energy loss due to pumping of these suspensions, we have just used high shear rate values to fit Bingham model as [34,79].

$$\tau = \mu_p \dot{\gamma} + \tau_y \tag{16}$$

τ refers to shear stress, μ_p is plastic viscosity, $\dot{\gamma}$ is shear rate, and τ_y is yield stress. Higher end for yield stress of catholyte and anolyte were estimated to be 204 Pa and 447 Pa respectively. Also, overlapping flow curve was observed for catholyte without any $Ni(OH)_2$ (in w/w_{water}% carbon black : Carbopol© = 14 : 1.4), indicating that about 2 orders of magnitude increase in yield stress compared to 1.4 w/w_{water}% Carbopol© in Figure 19 is mainly contributed by presence of carbon black in the suspension.

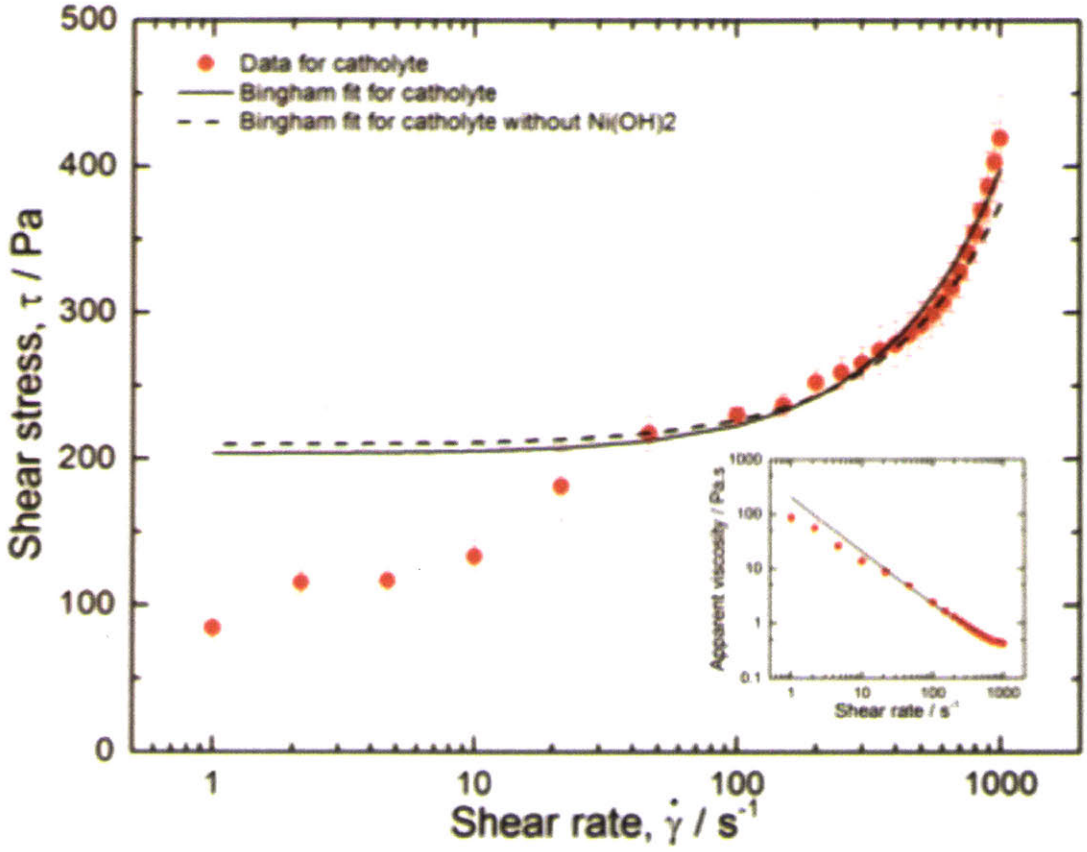

Figure 28: Flow curve of catholyte (in w/w_{water}% carbon black : $Ni(OH)_2$: Carbopol© = 14 : 39.8 : 1.4). Parameters fitted using Bingham model for high shear rate > 45 s^{-1} is given by $\mu_p = 0.2$ Pa. s, $\tau_y = 204$ Pa at $R^2 = 0.97$. Parameters for same catholyte without addition of any $Ni(OH)_2$ (in w/w_{water}% carbon black : Carbopol© = 14 : 1.4) is given by $\mu_p = 0.2$ Pa. s, $\tau_y = 210$ Pa at $R^2 = 0.99$. Apparent viscosity ($\eta = \tau/\dot{\gamma}$) is shown in inset.

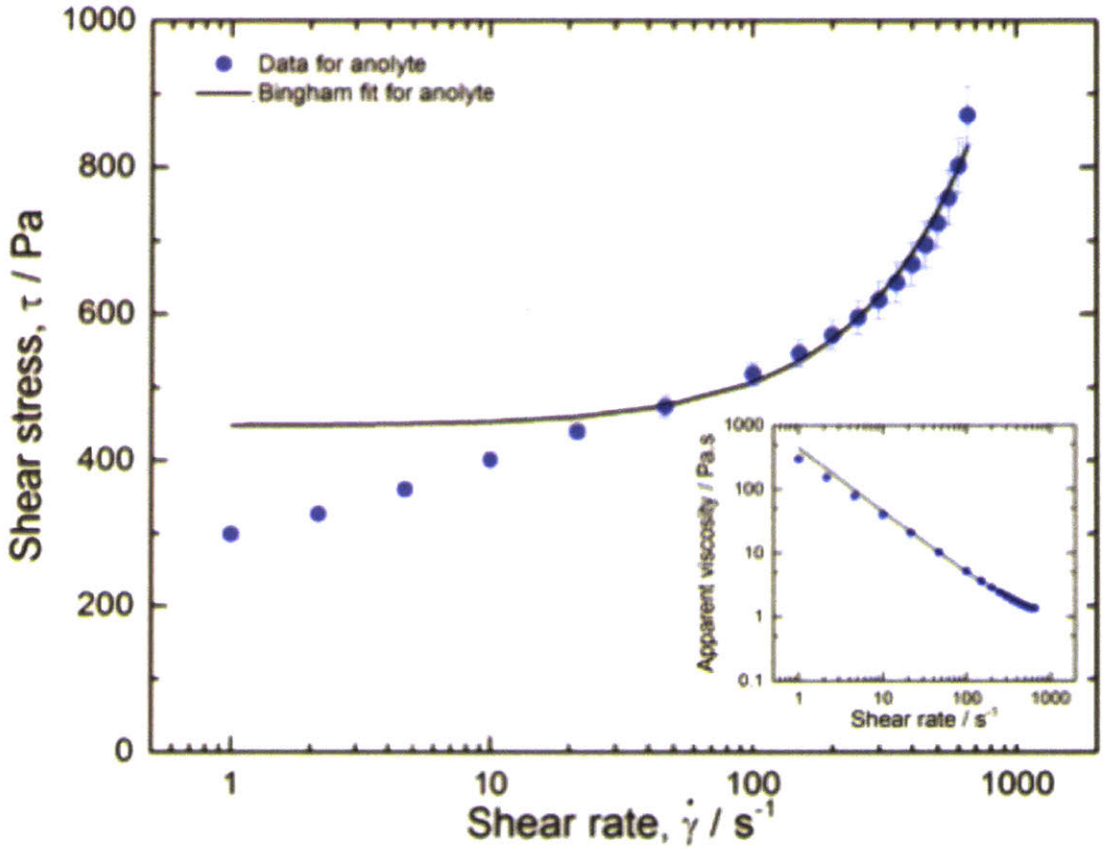

Figure 29: Flow curve of anolyte (in w/w_{water}% Zn : ZnO : Carbopol© = 71.1 : 42.1 : 1.8). Parameters fitted using Bingham model for high shear rate > 100 s^{-1} is given by $\mu_p = 0.6$ Pa. s, $\tau_y = 447$ Pa at $R^2 = 0.97$. Apparent viscosity ($\eta = \tau/\dot{\gamma}$) is shown in inset.

3.4.2 Energy loss calculations for wide and multichannel flow battery stack

Pressure drop ΔP due to pumping Bingham model-fluid through a channel can be simplified as [79]

$$\Delta P = \frac{3}{2B} L \left(Q \frac{\mu_p}{WB^2} + \tau_y \right) \tag{17}$$

where Q is the flow rate, L, $2B$, W are length, thickness and width of the channels respectively. When the same flow is divided into n parallel channels, ΔP is given by

$$\Delta P = \frac{3}{2B}\frac{L}{n}\left(\frac{Q}{n}\frac{\mu_p}{WB^2} + \tau_y\right) \tag{18}$$

Here, Q is the total flow rate, L total length of all channels. Hence, energy efficiency loss due to pumping for continuous channel flow of Bingham model-fluid can be simplified as

$$\eta_{pump}(\%) = \frac{3}{2B}\frac{L}{n}\left(\frac{Q}{n}\frac{\mu_p}{WB^2} + \tau_y\right)\frac{1}{E_{density}} \times 100\% \tag{19}$$

Thickness $2B$ of the channel was set at 2 mm in the calculation. L is adjusted such that it meets 1 kW power output requirement for power density of 10 mW/cm^2. Here, Q is calculated from volume of catholyte needed and time of battery discharge. Figure 30 shows how energy efficiency loss due to pumping changes with width and number of parallel channels in the battery stack for catholyte (in w/w_{water}% carbon black : $Ni(OH)_2$: Carbopol© = 14 : 39.8 : 1.4). By designing a stack with multiple channels and larger dimensions, energy loss due to pumping can be reduced. For example, by using 20 of 3 cm wide channel, energy loss can be easily minimized to < 1%. These number decrease even further when the number of channels is increased, as the length of each channel decreases. This analysis highlights the importance of including battery stack design considerations while designing semi-solid flow battery prototypes.

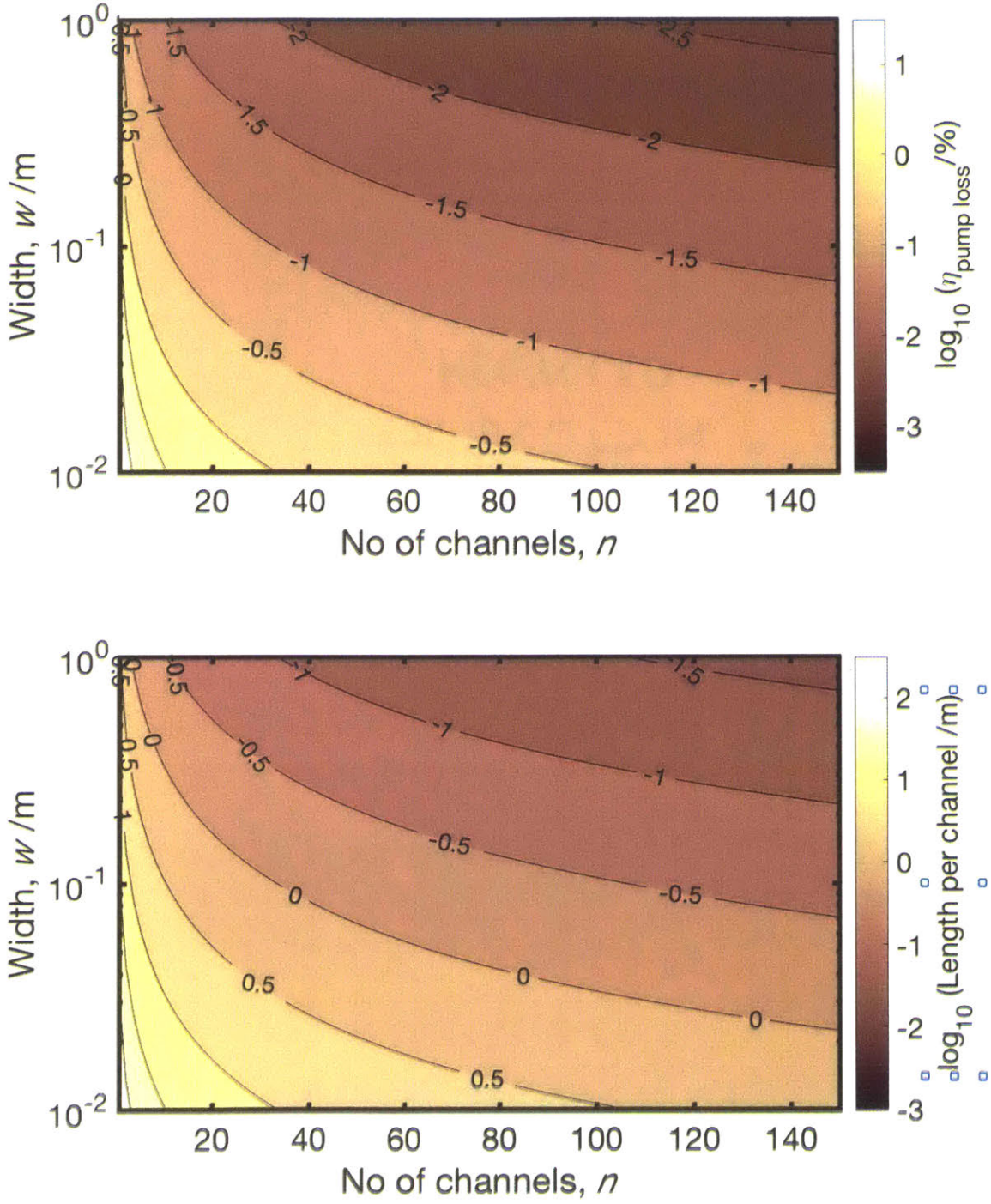

Figure 30: (top) Estimated efficiency loss due to pumping; (bottom) Length per channel needed to pump catholyte (in w/w_{water}% carbon black : $Ni(OH)_2$: Carbopol© = 14 : 39.8 : 1.4).The contour

represents order of magnitude of efficiency lost due to pumping and length per channel (in m) respectively. The stack dimensions were assumed to have 1 kW output. Energy density of the catholyte (85 $Wh/L_{catholyte}$) and power density (30 mW/cm^2) were taken from Figure 27.

3.4.3 Bingham number and plug flow visualization

Plug flow refers to solid-like flow of suspension. Plug flow of suspension is important for highly energy efficient semi-solid flow battery, as it minimizes retention of charged or discharged particles within the flow channel due to non-uniform flow as one would find in Newtonian or low yield stress fluids [80]. There are two methods to improve uniformity of flow field of the suspension: 1) induce slip at the wall, 2) design an elastic stress dominated flow, in other words, flow with high Bingham number. Bingham number *Bn* is defined as ratio of elastic to viscous stress (ratio of second and first term in the bracket of Equation 19), and can be expressed as

$$Bn = \tau_y / \left(\frac{Q\mu_p}{WB^2}\right) \tag{20}$$

As shown in Figure 31, yield stress of the suspension also helps to maintain high Bingham number (>10) during continuous flow. Figure 32 shows flow field visualization for catholyte without $Ni(OH)_2$ (composition in w/w_{water}% carbon black : Carbopol© = 14 : 1.4) at 0.5 mL/min (*Bn* ~ 2700) and 4.0 mL/min (*Bn* ~ 600), and water at 4.0 mL/min (*Bn* = 0). As, one may expect, presence of yield stress causes the catholyte to flow with uniform velocity distribution in the channels, however, Newtonian fluid like water has parabolic velocity profile.

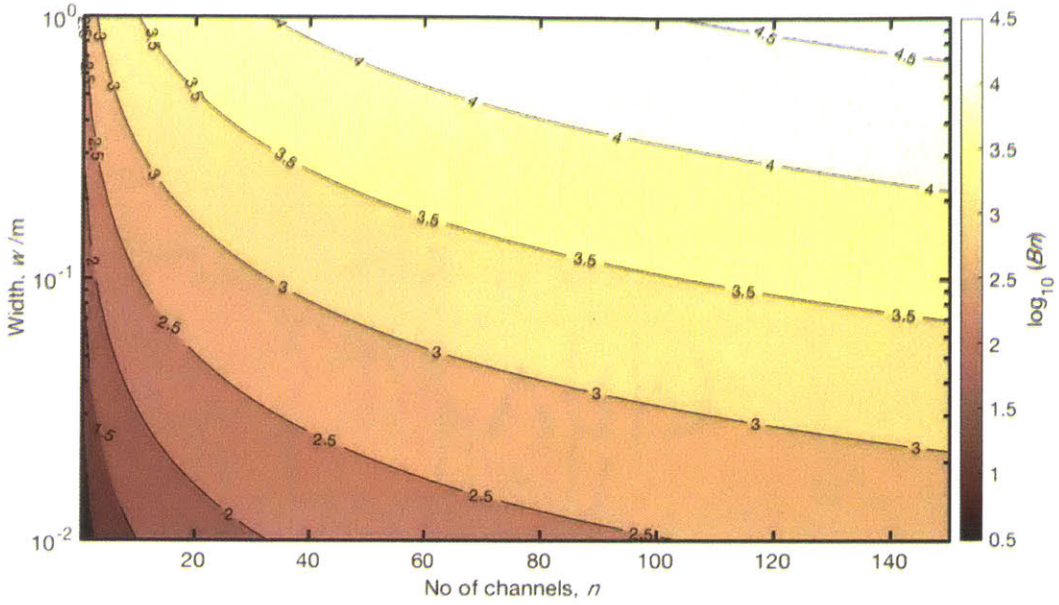

Figure 31: Bingham number (*Bn*) of flows calculated in Figure 30. The contour represents order of magnitude of *Bn*.

With that said, although we are able to achieve uniform flow field and find strategies to minimize energy loss within the flow channel, energy loss in manifolds and during flow division is not considered here. Lubricant Impregnated Surface (LIS) as such implemented by Varanasi et al. will be useful for these purposes [81].

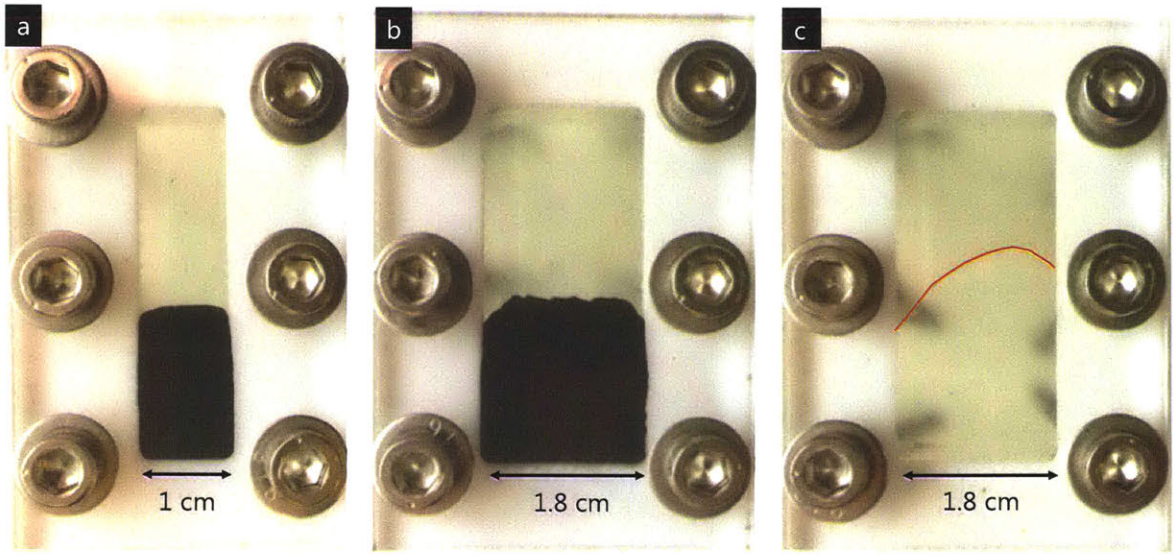

Figure 32: Flow profile for catholyte (composition in w/w_{water}% carbon black : Carbopol© = 14 : 1.4) at a) 0.5 mL/min ($Bn \sim 2700$) , b) 4.0 mL/min ($Bn \sim 600$) and c) water at 4.0 mL/min ($Bn = 0$). Thickness of the channel is 1.5 mm. Flow profile for water is highlighted with red line. Uniform flow profile is observed for the catholyte with yield stress and parabolic flow profile observed for water.

3.5 Flow cell design and performance

When a conductive suspension is charged or discharged in an open cell (i.e. active material extends to regions outside of electroactive zone), there are chances the extended suspension to be discharged too[60]. Hence, best performance of the suspension was first evaluated in a simple closed cell as discussed in sections 3.2 and 3.3. In this section, performance of the suspension in flow cell will be discussed. Two flow cells were designed for this study (Figure 33 and Figure 34). In both cases, suspension was pumped into the channel once and galvanostatic charge discharge was performed in static mode.

Design 1 (Figure 33) was made of conductive graphite frame and had narrow channel. Conductive frame causes the conductive suspension further from the separator to be active too. Hence, voltage efficiency subsequently energy efficiency, E.E of the battery is reduced to 44% (Figure 33) compared to 84% in static closed cell at 2 mA/cm2 (Figure 26). Energy efficiency here is defined as ratio of energy required to charge to energy gained from discharge.

$$E.E = \frac{\int V\, dQ_{discharge}}{\int V\, dQ_{charge}} \times 100\% \tag{21}$$

Improved design 2 (Figure 34) had non-conductive frame and wide channel. The non-conductive frame was intended to reduce the effect of electroactive zone extension and the wide channel design was to mimic wide channel design proposed in section 0. Due to complicated designs of the Design 2 cell, it was fabricated using 3-D printer, and clear resin was used to able to monitor flow of suspension into the cell. At the same current density, higher energy efficiency, E.E, 70% was achieved.

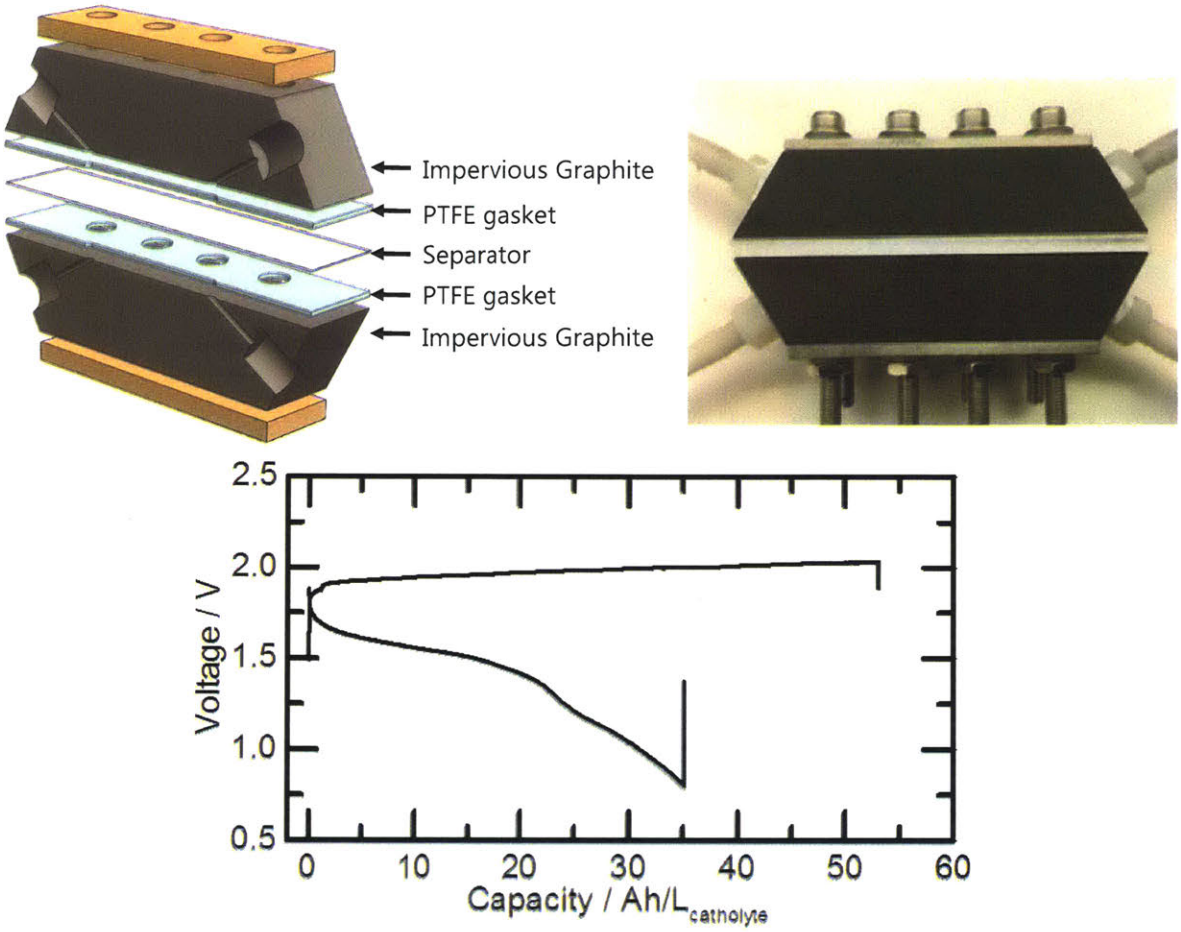

Figure 33: Flow cell design 1 with conductive frame and narrow channel and its electrochemical performance. Both anolyte and catholyte channels were 3 mm wide, 1.5 mm thick and 3 cm long. Impervious graphite (Fuel Cell Store, USA) was used as current collector on both sides. Catholyte composition (in w/w_{water}% carbon black : $Ni(OH)_2$: Carbopol© = 14 : 39.8 : 1.4). Anolyte composition (in w/w_{water}% Zn : ZnO : Carbopol© = 71.1 : 31.3 : 1.8). Charge-discharge was performed at 2 mA/cm^2.

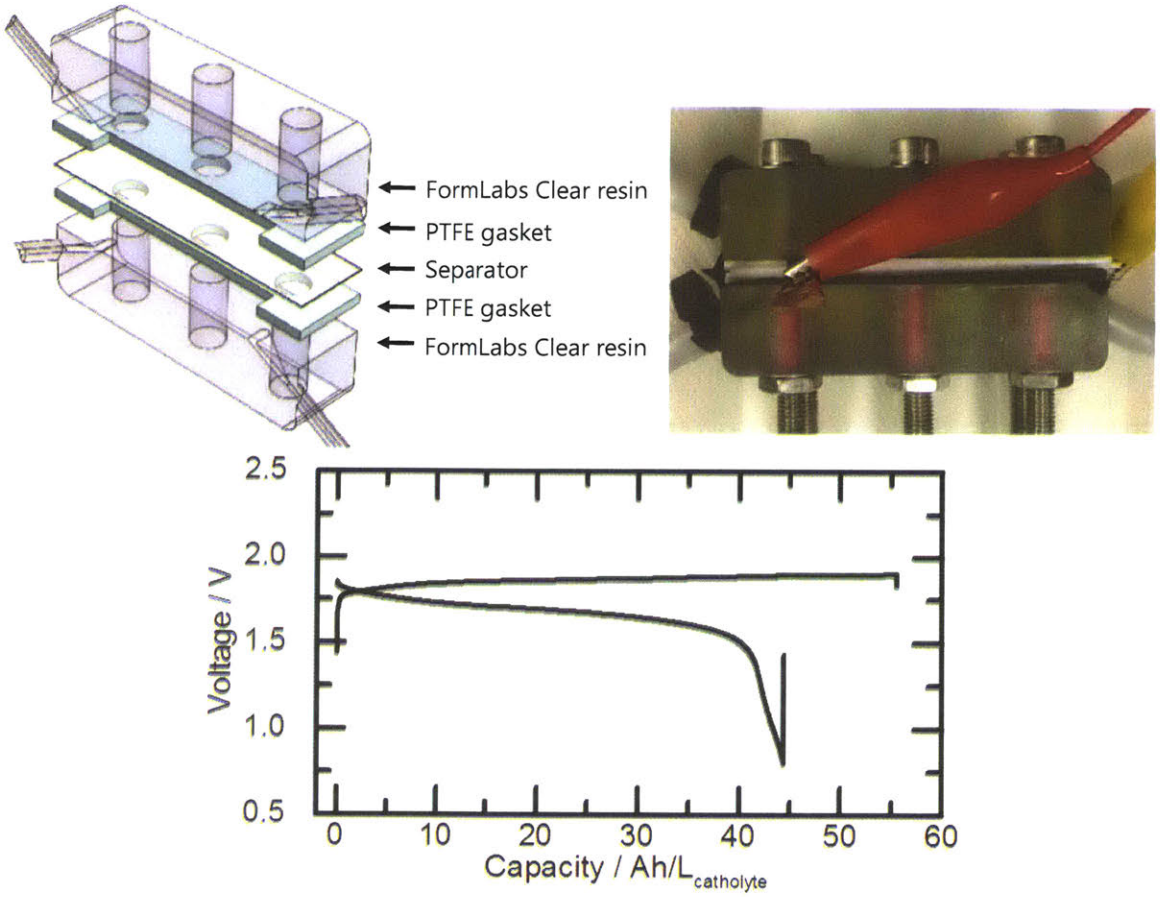

Figure 34: Flow cell design 2 with non-conductive frame and wide channel and its electrochemical performance. Both anolyte and catholyte channels were 9 mm wide and 4 cm long. Anolyte and catholyte channels had 3.0 and 1.5 mm thickness respectively. Impervious graphite (Fuel Cell Store, USA) was used as current collector for catholyte and brass plate (McMaster Carr, USA) was used as current collector for anolyte. The current collectors were inserted in between the gasket and frame. Catholyte composition (in w/w_{water}% carbon black : $Ni(OH)_2$: Carbopol© = 14 : 39.8 : 1.4). Anolyte composition (in w/w_{water}% Zn : ZnO : Carbopol© = 71.1 : 31.3 : 1.8). Charge-discharge was performed at 2 mA/cm^2.

4. Conclusions

In this work, we have shown how to systematically design semi-solid electrode for flow battery. There are three critical parameters that determine performance of semi-solid electrode: stability, conductivity and flowability.

In Chapter 3.1, we have shown how interplay of different forces acting on particle determines the stability of the catholyte and anolyte, and why designing mechanical structure "yield stress" within the electrolyte is important to suspend large particles such as zinc (~100 micron) and $Ni(OH)_2$ (~10 micron). We added 1.4 w/w_{water}% Carbopol© for the catholyte and 1.8 w/w_{water}% Carbopol© for the anolyte. These gels had yield stress of 0.7 Pa and 7 Pa respectively, which was suffice to suspend the large particles.

In Chapter 3.2, we highlighted the importance of identifying percolation threshold of conductive additive, not just to minimize material usage, but also to access full capacity of the active material. Percolation threshold for carbon black in catholyte was 6 w/w_{water}% and for Zn in anolyte was 48 w/w_{water}%. For the catholyte, above the percolation threshold, conductivity exhibited power-law increase $\sigma_e \sim (\phi - \phi_c)^s$, with conductivity percolation index $s \sim 1.32$. Discharge capacity of Ni(OH)2 increased with concentration of carbon black above the percolation threshold, and reached a constant value after 10 w/w_{water}% carbon black, where, electrical conductivity was in $\sigma_e \sim \phi^s$ percolation regime. Ratio of discharge capacity of Ni(OH)2 under two different discharge plateaus also found to change with carbon black concentration. Near percolation threshold, capacity from high potential (till ~1.1 V) plateau was smaller than the capacity from low potential (1.1~0.8 V) discharge plateau. As concentration of carbon black is increased this ratio was smaller. At 6 w/w_{water}% and 14 w/w_{water}% carbon black, the high potential capacity to low potential ratio was 0.6 : 0.29 and 0.83 : 0.05. This trend was explained using

Delmas et al.'s postulation on how poor coverage of conductive additive on the $Ni(OH)_2$ can cause larger capacity from the lower potential discharge plateau [76].

In Chapter 3.3, since we know the optimum concentration for conductive additive in the suspensions, we then use the same conductive additive composition (14 w/w_{water}% carbon black) with larger (39.8 w/w_{water}%) concentration of $Ni(OH)_2$ to test high energy density and power density capability of the catholyte. Highest catholyte energy density achieved was 134 $Wh/L_{catholyte}$, which is ~ 3 times higher than state of the art vanadium flow battery. Highest power density achieved was 78.5 mW/cm^2, which was close to power density of continuous flow mode vanadium flow battery (~200 mW/cm^2).

In Chapter 3.4, we then tested flowability of the chosen suspension composition and discussed strategies to minimize pumping loss, while utilizing yield stress of these suspensions for our advantage. Flow curve was measured for catholyte and anolyte with highest amount of active material prepared in this study. Catholyte composition was (in w/w_{water}%) carbon black : $Ni(OH)_2$: Carbopol© = 14 : 39.8 : 1.4 and anolyte composition was Zn : ZnO : Carbopol© = 71.1 : 42.1 : 1.8. The stress response to high shear rate were fitted to Bingham model and higher estimate for yield stress was obtained. Bingham yield stress for catholyte and anolyte was 204 Pa and 447 Pa respectively. Energy loss for continuous pumping the catholyte into the channels of 1 kW flow stack was then calculated. We took lower estimate of power density of 10 mW/cm^2 to calculate the cell dimension needed. By designing wide channels in parallel flow, we found that energy loss due to pumping can be minimized to < 1% during continuous flow. We also experimental photographs of uniform flow profile in yield stress possessing catholyte used in this study and parabolic flow profile of water pumped at the same flow rate. The uniform flow profile of catholyte

was due to dominance of elastic stress over viscous stress in the flow and can minimize used active material retention in the channel during operation as suggested by Smith et al. [80].

5. *Future work and open questions*

This section will be divided into two larger pictures: 1) What can be done to further understand and improve Zn-$Ni(OH)_2$ semi-solid battery system; 2) What future work holds for semi-solid flow battery research.

Firstly, on what can be done to further improve present Zn-Ni alkaline semi-solid battery system. At the suspension level, the system has been optimized for catholyte, further work has to be done to optimize the anolyte. Anolyte used in this study has large energy density, while still has the ability to flow. It is possible because, Zn particles do not have fractal structures are carbon black as shown in this study. Hence, more work has to be done to further utilize the anolyte suspension. Systematic studies on electrochemical performance of anolyte with varying concentration of Zn will help to minimize density and material cost of the suspension. Also, studies on quantifying corrosion rate of anolyte is important for safety purposes and improving cyclability of the battery. Several strategies can be applied to decrease the corrosion rate of anolyte such as addition of $Ca(OH)_2$[45], KF or K_2CO_3[46]. At high current densities, poor non-uniform electroplating of Zn on the current collector during charging process, reduces the cyclability of the system. Usage of polymer additives that adsorb on the surface of Zn particles and the current collector[82], or pulsed charging technique may alleviate this problem[83].

In general, variety other different chemistries can also be tried with semi-solid flow battery technique. Strategies provided above is applicable to creating stable and high energy density suspensions in both aqueous and non-aqueous electrolytes. Hence, low voltage and thermodynamically-stable (within 1.23 V window) chemistries are suitable to be tested for semi-solid flow battery technology.

As mentioned in Chapter 3.4, although having yield stress helps create uniform flow and energy efficiency loss due to pumping can be minimized to as low as 0.1% by selecting the right dimension of the flow stack, there are still practical challenges in making and operating a flow cell stack. Yield stress fluids require tangential velocity to be maintained to continuously flow[84]. This complicates flow division from manifold into multiple channels of flow stack. The open question is two-dimensional flow is the way to scale-up semi-solid flow battery?

Another way to alleviate high yield stress problem is to find what is the optimum yield stress that is high enough to allow plug flow for a given dimension of the channel and low enough for the flow to be divided into different channels without any blocked manifolds. Obviously, these are complex engineering problems, however, any fundamental work on developing theories and experiments for expansion and contraction flows[85], mold filling flow[86] of yield stress fluids from the rheology community may be useful to give better idea of how to design scalable flow battery stack.

6. *References*

1. International Energy Agency. *Renewables 2017: Analysis and forecasts to 2022*. (International Energy Agency).
2. Huff, G. *et al.* DOE/EPRI 2013 electricity storage handbook in collaboration with NRECA. *Report SAND2013- \ldots* 340 (2013). doi:SAND2013-5131
3. Winter, M. & Brodd, R. J. What Are Batteries, Fuel Cells, and Supercapacitors? *Chemical Reviews* **104,** 4245–4270 (2004).
4. Bard, A. J., Faulkner, L. R., Leddy, J., & Zoski, C. G. *Electrochemical methods: fundamentals and applications*. (1980).
5. Renewables 2017. Available at: https://www.iea.org/publications/renewables2017/#section-4-1. (Accessed: 11th August 2018)
6. Daniel, C. Materials and processing for lithium-ion batteries. *JOM* **60,** 43–48 (2008).
7. Choi, J. W. & Aurbach, D. Promise and reality of post-lithium-ion batteries with high energy densities. *Nature Reviews Materials* **1,** 16013 (2016).
8. Soloveichik, G. L. Flow Batteries: Current Status and Trends. *Chemical Reviews* **115,** 11533–11558 (2015).
9. Park, M., Ryu, J., Wang, W. & Cho, J. Material design and engineering of next-generation flow-battery technologies. *Nature Reviews Materials* **2,** 16080 (2016).
10. Thaller, L. H. Electrically rechargeable REDOX flow cell. (1976).
11. Li, Z. *et al.* Air-Breathing Aqueous Sulfur Flow Battery for Ultralow-Cost Long-Duration Electrical Storage. *Joule* **1,** 306–327 (2017).
12. Skyllas-Kazacos, M., Rychick, M. & Robins, R. All-vanadium redox battery. (1988).

13. Li, L. *et al.* A Stable Vanadium Redox-Flow Battery with High Energy Density for Large-Scale Energy Storage. *Advanced Energy Materials* **1,** 394–400 (2011).

14. Duduta, M. *et al.* Semi-solid lithium rechargeable flow battery. *Advanced Energy Materials* **1,** 511–516 (2011).

15. Kim, S. *et al.* 1 kW/1 kWh advanced vanadium redox flow battery utilizing mixed acid electrolytes. *Journal of Power Sources* **237,** 300–309 (2013).

16. Hopkins, B. J., Smith, K. C., Slocum, A. H. & Chiang, Y. M. Component-cost and performance based comparison of flow and static batteries. *Journal of Power Sources* **293,** 1032–1038 (2015).

17. Marsal, P. A., Karl, K. & Urry, L. F. Dry cell. (1960).

18. *Sonneveld (1991) The zinc suspension electrode.pdf.*

19. Hatzell, K. B., Boota, M. & Gogotsi, Y. Materials for suspension (semi-solid) electrodes for energy and water technologies. *Chem. Soc. Rev.* **44,** 8664–8687 (2015).

20. Fan, F. Y. *et al.* Polysulfide flow batteries enabled by percolating nanoscale conductor networks. *Nano Letters* **14,** 2210–2218 (2014).

21. Zhang, Y., Narayanan, A., Mugele, F., Cohen Stuart, M. A. & Duits, M. H. G. Charge inversion and colloidal stability of carbon black in battery electrolyte solutions. *Colloids and Surfaces A: Physicochemical and Engineering Aspects* **489,** 461–468 (2016).

22. Parant, H. *et al. Flowing suspensions of carbon black with high electronic conductivity for flow applications: Comparison between carbons black and exhibition of specific aggregation of carbon particles.* **119,** (2017).

23. Li, Z. *et al.* Aqueous semi-solid flow cell: demonstration and analysis. *Physical chemistry chemical physics : PCCP* **15,** 15833–9 (2013).

24. Hatzell, K. B. *et al.* Direct observation of active material interactions in flowable electrodes using X-ray tomography. *Faraday Discussions* **199,** 511–524 (2017).

25. Hatzell, K. B. *et al.* Composite manganese oxide percolating networks as a suspension electrode for an asymmetric flow capacitor. *ACS Applied Materials and Interfaces* **6,** 8886–8893 (2014).

26. Hatzell, K. B., Boota, M., Kumbur, E. C., Gogotsia, Y. & Gogotsi, Y. Flowable conducting particle networks in redox-active electrolytes for grid energy storage. *Journal of the Electrochemical Society* **162,** A5007–A5012 (2015).

27. Parant, H. *et al.* Flowing suspensions of carbon black with high electronic conductivity for flow applications: Comparison between carbons black and exhibition of specific aggregation of carbon particles. *Carbon* **119,** 10–20 (2017).

28. Cerbelaud, M. *et al.* Numerical and experimental study of suspensions containing carbon blacks used as conductive additives in composite electrodes for lithium batteries. *Langmuir* **30,** 2660–2669 (2014).

29. Wei, T. S. *et al.* Biphasic Electrode Suspensions for Li-Ion Semi-solid Flow Cells with High Energy Density, Fast Charge Transport, and Low-Dissipation Flow. *Advanced Energy Materials* **5,** 1–7 (2015).

30. Stauffer, D. Scaling Theory of Percolation Clustgers. *Physics Reports-Review Section of Physics Letters* **54,** 1–74 (1979).

31. Hatzell, K. B. *et al.* Direct observation of active material interactions in flowable electrodes using X-ray tomography. *Faraday Discussions* **199,** 511–524 (2017).

32. Helal, A. H. Designing devices using electro-active yield stress fluids by. (2016).

33. Richards, J. J., Hipp, J. B., Riley, J. K., Wagner, N. J. & Butler, P. D. Clustering and Percolation in Suspensions of Carbon Black. *Langmuir* **33,** 12260–12266 (2017).

34. Chen, X. *et al.* A low-dissipation, pumpless, gravity-induced flow battery. *Energy Environ. Sci.* **9,** 1760–1770 (2016).

35. Trappe, V., Prasad, V., Cipelletti, L., Segre, P. N. & Weitz, D. A. Jamming phase diagram for attractive particles. *Nature* **411,** 772–775 (2001).

36. Bonn, D., Denn, M. M., Berthier, L., Divoux, T. & Manneville, S. Yield stress materials in soft condensed matter. *Reviews of Modern Physics* **89,** 1–40 (2017).

37. Schall, P. & van Hecke, M. Shear Bands in Matter with Granularity. *Annual Review of Fluid Mechanics* **42,** 67–88 (2010).

38. Cloitre, M. Yielding, Flow, and Slip in Microgel Suspensions: From Microstructure to Macroscopic Rheology. in *Microgel Suspensions* 283–309 (Wiley-Blackwell, 2011). doi:10.1002/9783527632992.ch11

39. Bird, R. B. *Dynamics of Polymeric Liquids.* (John Wiley & Sons, Inc, 1977).

40. Fredrickson, A. & Bird, R. B. Non-Newtonian Flow in Annuli. *Ind. Eng. Chem.* **50,** 347–352 (1958).

41. Linden, D. & Reddy, T. *Handbook of Batteries.* (McGraw Hill Professional, 2001).

42. Olivetti, E. A., Ceder, G., Gaustad, G. G. & Fu, X. Lithium-Ion Battery Supply Chain Considerations: Analysis of Potential Bottlenecks in Critical Metals. *Joule* **1,** 229–243 (2017).

43. Bonnick, P. *Development of a Lab-Scale, Rechargeable, Aqueous Coin Cell and Methods for Measuring the Self-Discharge Rate of Zinc Electrodes.* (2015).

44. Turney, D. E. *et al.* Rechargeable zinc alkaline anodes for long-cycle energy storage Rechargeable zinc alkaline anodes for long-cycle energy storage. *Chemistry of Materials* (2017). doi:10.1021/acs.chemmater.7b00754

45. Sharma, R. A. Physico-Chemical Properties of Calcium Zincate. *J. Electrochem. Soc.* **133,** 2215–2219 (1986).

46. McLarnon, F. R. The Secondary Alkaline Zinc Electrode. *Journal of The Electrochemical Society* **138,** 645 (1991).

47. Micro X-ray Computed Tomography (CT) Scanning & Analysis. Available at: https://www.exponent.com/services/practices/engineering/polymer-science--materials-chemistry/capabilities/micro-xray-computed-tomography-ct-scanning--anal__. (Accessed: 11th August 2018)

48. Bode, H., Dehmelt, K. & Witte, J. Zur kenntnis der nickelhydroxidelektrode—I.Über das nickel (II)-hydroxidhydrat. *Electrochimica Acta* **11,** 1079-IN1 (1966).

49. Van der Ven, A., Morgan, D., Meng, Y. S. & Ceder, G. Phase Stability of Nickel Hydroxides and Oxyhydroxides. *Journal of The Electrochemical Society* **153,** A210 (2006).

50. *McBreen (2011) Handbook of battery materials.pdf.*

51. *Barnard (1980) The cause of residual capacity in nickel oxyhydroxide electrodes.pdf.*

52. Oliva, P. *et al. Review of the structure and the electrochemistry of nickel hydroxides and oxy-hydroxides.* **8,** (1982).

53. Mo, Y., Hwang, E. & Scherson, D. A. In Situ Quarlz Crystal Microbalance Studies of Nickel Hydrous Oxide Films in Alkaline Electrolytes. *J. Electrochem. Soc.* **143,** 7 (1996).

54. Bardé, F., Palacin, M. R., Chabre, Y., Isnard, O. & Tarascon, J.-M. In Situ Neutron Powder Diffraction of a Nickel Hydroxide Electrode. *Chemistry of Materials* **16,** 3936–3948 (2004).

55. Léger, C., Tessier, C., Ménétrier, M., Denage, C. & Delmas, C. Investigation of the Second Discharge Plateau of the beta(III)-NiOOH / beta(II) -Ni (OH)2 System. *Journal of The Electrochemical Society* **146,** 924–932 (1999).

56. Sac-Epée, N. On the Origin of the Second Low-Voltage Plateau in Secondary Alkaline Batteries with Nickel Hydroxide Positive Electrodes. *Journal of The Electrochemical Society* **144,** 3896 (1997).

57. Kim, M.-S., Hwang, T.-S. & Kim, K.-B. A Study of the Electrochemical Redox Behavior of Electrochemically Precipitated Nickel Hydroxides Using Electrochemical Quartz Crystal Microbalance. *J. Electrochem. Soc.* **144,** 1537–1543 (1997).

58. Barnard, R., Crickmore, G. T., Lee, J. A. & Tye, F. L. The cause of residual capacity in nickel oxyhydroxide electrodes. *Journal of Applied Electrochemistry* **10,** 61–70 (1980).

59. Liu, J. & Wang, Y. Preliminary study of high energy density Zn/Ni flow batteries. *Journal of Power Sources* **294,** 574–579 (2015).

60. Smith, K. C., Brunini, V. E., Dong, Y., Chiang, Y. M. & Carter, W. C. Electroactive-zone extension in flow-battery stacks. *Electrochimica Acta* **147,** 460–469 (2014).

61. Larson, R. G. *The structure and rheology of complex fluids. The Structure and Rheology of Complex Fluids* (Oxford University Press, 1999).

62. Barnes, H. A., Hutton, J. F. & Walters, K. *An Introduction to Rheology*. (Elsevier B.V, 1993).

63. Beris, A. N., Tsamopoulos, J. A., Armstrong, R. C. & Brown, R. A. Creeping motion of a sphere through a Bingham plastic. *Journal of Fluid Mechanics* **158,** 219–244 (1985).

64. Piau, J. M. Carbopol gels: Elastoviscoplastic and slippery glasses made of individual swollen sponges. Meso- and macroscopic properties, constitutive equations and scaling laws. *Journal of Non-Newtonian Fluid Mechanics* **144,** 1–29 (2007).

65. Bonn, D., Denn, M. M., Berthier, L., Divoux, T. & Manneville, S. Yield stress materials in soft condensed matter. *Reviews of Modern Physics* **89,** 1–40 (2017).

66. Emady, H., Caggioni, M. & Spicer, P. Colloidal microstructure effects on particle sedimentation in yield stress fluids. *Journal of Rheology* **57,** 1761–1772 (2013).

67. Machell, G. & Richards, G. N. The Alkaline Degradation of Polysaccharides. Part III. *Journal of the Chemical Society* 1199–1204 (1958). doi:10.1039/JR9580001199

68. Marsal, P. A., Kordesch, K. & Urry, L. F. Dry cell. (1960).

69. Cloitre, M. & Bonnecaze, R. T. A review on wall slip in high solid dispersions. *Rheologica Acta* **56,** 283–305 (2017).

70. Oppong, F. K. & de Bruyn, J. R. Mircorheology and jamming in a yield-stress fluid. *Rheologica Acta* **50,** 317–326 (2011).

71. Fan, F. Y. *et al.* Polysulfide flow batteries enabled by percolating nanoscale conductor networks. *Nano Letters* **14,** 2210–2218 (2014).

72. Kirkpatrick, S. Percolation and Conduction. *Reviews of Modern Physics* **45,** 574–588 (1973).

73. Helal, A., Divoux, T. & McKinley, G. H. Simultaneous Rheoelectric Measurements of Strongly Conductive Complex Fluids. *Physical Review Applied* **6,** 1–19 (2016).

74. Richards, J. J., Hipp, J. B., Riley, J. K., Wagner, N. J. & Butler, P. D. Clustering and Percolation in Suspensions of Carbon Black. *Langmuir* **33,** 12260–12266 (2017).

75. Rintoul, M. D. & Torquato, S. Precise determination of the critical threshold and exponents in a three-dimensional continuum percolation model. *Journal of Physics A: Mathematical and General* (1997). doi:10.1088/0305-4470/30/16/005

76. Léger, C., Tessier, C., Ménétrier, M., Denage, C. & Delmas, C. Investigation of the Second Discharge Plateau of the beta(III)-NiOOH / beta(II) -Ni (OH)2 System. *Journal of The Electrochemical Society* **146,** 924–932 (1999).

77. Shukla, G., Del Olmo Diaz, D., Thangavel, V. & Franco, A. A. Self-Organization of Electroactive Suspensions in Discharging Slurry Batteries: A Mesoscale Modeling Investigation. *ACS Applied Materials and Interfaces* (2017). doi:10.1021/acsami.7b02567

78. Stauffer, D. Scaling Theory of Percolation Clustgers. *Physics Reports-Review Section of Physics Letters* **54,** 1–74 (1979).

79. Bird, R. B. *Dynamics of Polymeric Liquids.* (John Wiley & Sons, Inc, 1977).

80. Smith, K. C., Chiang, Y.-M. & Craig Carter, W. Maximizing Energetic Efficiency in Flow Batteries Utilizing Non-Newtonian Fluids. *Journal of The Electrochemical Society* **161,** A486–A496 (2014).

81. Solomon, B. R. Butterflies and Batteries: Advances in Liquid Repellent Surfaces by Anisotropic Wetting and Lubricant Impregnation by. (2016).

82. Banik, S. J. & Akolkar, R. Suppressing Dendrite Growth during Zinc Electrodeposition by PEG-200 Additive. *Journal of the Electrochemical Society* **160,** D519–D523 (2013).

83. Garcia, G., Ventosa, E. & Schuhmann, W. Complete Prevention of Dendrite Formation in Zn Metal Anodes by Means of Pulsed Charging Protocols. *ACS Applied Materials & Interfaces* **9,** 18691–18698 (2017).

84. Denn, M. M. & Bonn, D. Issues in the flow of yield-stress liquids. *Rheol Acta* **50,** 307–315 (2011).

85. de Souza Mendes, P. R., Naccache, M. F., Varges, P. R. & Marchesini, F. H. Flow of viscoplastic liquids through axisymmetric expansions–contractions. *Journal of Non-Newtonian Fluid Mechanics* **142,** 207–217 (2007).

86. Oda, K., White, J. L. & Clark, E. S. Jetting phenomena in injection mold filling mold filling. *Polymer Engineering & Science* **16,** 585–592 (1976).